Plant Physiology®

Causes and consequences of endogenous hypoxia on growth and metabolism of developing maize kernels

Matthias Langer, Alexander Hilo, Islahn-Chou Guan, Karen E. Koch, Hui Xiao, Hui Xiao, Alexander Hilo, Steffen Wagner, Stefan Ortleb, Volodymyr Radchuk, Simon Mayer, Alexander, Islahn-Chou Guan, Stefan Ortleb, Alexander, Stefan Ortleb, Stefan Ortl

- 1 Molecular Genetics Department, Leibniz-Institut für Pflanzengenetik und Kulturpflanzenforschung, Corrensstrasse, 06466 Seeland-Gatersleben, Germany
- 2 University of Florida, Horticultural Sciences Department, Fifield Hall, 2550 Hull Rd., PO Box 110690, Gainesville, Florida, 32611, USA
- 3 Biosystems Department, KU Leuven—University of Leuven, BIOSYST-MeBioS, Willem de Croylaan 42, B-3001 Leuven, Belgium

*Author for correspondence: rollet@ipk-gatersleben.de (H.R.), borysyuk@ipk-gatersleben.de (L.B.)

M.L. performed oxygen profiling, respiration assays, in vitro assays, molecular and histological work, and all experimental treatments. H.X. performed the μ -CT, analyzed the images, and performed the gas transport simulations. P.V. and B.N. contributed to the draft of the manuscript. J.C.G. and K.E.K. analyzed RNA-Seq data and contributed to the draft of the manuscript. A.H. and H.R. performed metabolite profiling and data analysis. A.G. performed microspectroscopy. S.O., S.W., and S.M. performed MRI/3D modeling. V.R. supervised molecular work. H.R. and L.B. designed the research, analyzed the data and wrote the paper.

The authors responsible for distribution of materials integral to the findings presented in this article in accordance with the policy described in the Instructions for Authors (https://academic.oup.com/plphys/pages/General-Instructions) are: Hardy Rolletschek rollet@ipk-gatersleben.de and Ljudmilla Borisjuk borysyuk@ipk-gatersleben.de

Abstract

Maize (Zea mays) kernels are the largest cereal grains, and their endosperm is severely oxygen deficient during grain fill. The causes, dynamics, and mechanisms of acclimation to hypoxia are minimally understood. Here, we demonstrate that hypoxia develops in the small, growing endosperm, but not the nucellus, and becomes the standard state, regardless of diverse structural and genetic perturbations in modern maize (B73, popcorn, sweet corn), mutants (sweet4c, glossy6, waxy), and non-domesticated wild relatives (teosintes and Tripsacum species). We also uncovered an interconnected void space at the chalazal pericarp, providing superior oxygen supply to the placental tissues and basal endosperm transfer layer. Modeling indicated a very high diffusion resistance inside the endosperm, which, together with internal oxygen consumption, could generate steep oxygen gradients at the endosperm surface. Manipulation of oxygen supply induced reciprocal shifts in gene expression implicated in controlling mitochondrial functions (23.6 kDa Heat-Shock Protein, Voltage-Dependent Anion Channel 2) and multiple signaling pathways (core hypoxia genes, cyclic nucleotide metabolism, ethylene synthesis). Metabolite profiling revealed oxygen-dependent shifts in mitochondrial pathways, ascorbate metabolism, starch synthesis, and auxin degradation. Long-term elevated oxygen supply enhanced the rate of kernel development. Altogether, evidence here supports a mechanistic framework for the establishment of and acclimation to hypoxia in the maize endosperm.

Introduction

The concentration of oxygen within the plant body integrates positional cues, metabolic state and environmental conditions. Local levels can be substantially different from ambient and dynamically fluctuate. This, in turn, affects

cell labor and fates (Hammarlund et al., 2020). When the oxygen supply falls below respiratory demands, this is usually called hypoxic stress (Sasidharan et al., 2021). A prominent example is the detrimental oxygen shortage in waterlogged tissues during flooding events, which causes substantial economic losses of maize (Zea mays) and other crops every year

(FAO 2015). Hypoxia also plays a signaling role in regular developmental programs. For maize, it was shown that hypoxia, arising naturally within growing anthers, acts as a positional cue regulating germ cell fate (Kelliher and Walbot, 2012). For Arabidopsis (Arabidopsis thaliana), data supported the proposal that meristems are enclosed in chronic hypoxic niches, affecting both shoot apices and root primordia (Shukla et al., 2019; Weits et al., 2019).

In recent years, there has been substantial progress in the understanding of a plant's capacity to sense and signal lowoxygen concentrations (van Dongen and Licausi, 2015; Lee and Bailey-Serres, 2019). A major step was the discovery of oxygen-dependent enzymes (plant cysteine oxidases) that repress the operation of transcription factors such as group VII Ethylene Response Factors (VII-ERFs) (Weits et al., 2014). Posttranslational modification of the VII-ERFs reduces their stability under oxic conditions, while protein stability increases under low-oxygen conditions. Upon transfer to the nucleus, the VII-ERFs up-regulate a suite of genes, based on specific promoter motifs (Gasch et al., 2016), which eventually triggers acclimation. In addition, a multitude of other oxygen-, redox- and energy-dependent shifts, including histone methylation, modulate the plant's hypoxic response (Lee and Bailey-Serres, 2019; Wagner et al., 2019; Meng et al., 2020; Sasidharan et al., 2021). Overall, a remarkable convergence of functional features is evident for the low-oxygen sensing/signaling among plants and animals (Hammarlund et al., 2020).

Developing seeds of our major crops, in particular cereal grains, generally have a strongly hypoxic interior as demonstrated for barley (Rolletschek et al., 2004), wheat (van Dongen et al., 2004), maize (Rolletschek et al., 2005) and rice (own unpublished data). Storage metabolism, assimilate uptake and energy state appear coordinated by the low internal oxygen conditions (for review, see Borisjuk and Rolletschek, 2009). As demonstrated for maize, severe hypoxia governs the endosperm in particular, where it has marked effects on assimilate partitioning and local ATP levels (Rolletschek et al., 2005). As compared with seeds of other crops, oxygen deprivation appeared particularly pronounced in the maize kernel and led to the hypothesis that evolution of this largest cereal grain may have involved special adaptations to generate and/or respond to endogenous oxygen limitation (Borisjuk and Rolletschek, 2009). However, a mechanistic understanding based on molecular data are currently lacking. There are several, important unknowns relating to maize kernel hypoxia: Which features drive the majority of endosperm (but not embryo) into severe hypoxia? Is this outcome a consequence of low surface/volume ratio or are specific (ultra-) structural features involved? Does oxygen depletion (in sensu energy limitation) alter local input into signaling systems, gene expression, and/or metabolic control? Possibly yes, since analysis of the endosperm interior showed an upregulation of RAP2.12 (RELATED TO APETALA2.12; an VII-ERF transcription factor) as well as hypoxia-responsive genes indicative of a fermentative metabolism in the center that did not extend to the periphery (Gayral et al., 2017). How are low-oxygen signals integrated into the normal developmental control of the kernel? As hypoxia is tightly interwoven with accumulation of both ethylene (Hartman et al., 2021) and reactive oxygen species (ROS; Schmidt et al., 2018), it is tempting to speculate that the ethylene-/ROS-mediated programed cell death during maize endosperm development (Young et al., 1997) is a direct consequence of hypoxia. Moreover, developmental progression, kernel size, and kernel composition might respond to a scenario where more/less oxygen becomes available.

To address above questions, we first investigated whether the endogenous hypoxic environment could be altered by genetic perturbations including distinct kernel types (popcorn, dent, sugary), maize mutants (glossy6, sweet4c, waxy) and wild relatives (teosintes and tripsacums) of modern maize lines, with focus on the model genotype B73. We applied oxygen profiling using microsensors to test if kernel anatomy or starch/sugar composition (defined by kernel type) are relevant features for endosperm hypoxia. By analyzing wild relatives, we tested if kernel hypoxia is merely a feature of domesticated (large-sized) maize kernels or also inherent to small-grained ancestors. Magnetic resonance imaging (MRI), enabling highresolution imaging of the seed interior, was used to check for moisture gradients, having potential relevance for gas diffusivity. By combining MRI with infrared microspectroscopy, we tested for the existence of lipidous layers, surrounding the endosperm and potentially hampering oxygen diffusion. To model the kernel ultrastructure (including porosity and oxygen diffusivity), we applied X-ray micro-computed tomography (µ-CT) and generated a 3D kernel model with spatial resolution of 5 µm. This was used to check for void spaces inside the kernel with relevance for oxygen diffusibility. The kernel's dynamic response to varying oxygen supply was studied at the molecular (RNA-sequencing) and biochemical (metabolite profiling) levels. The search for reciprocally responding genes and metabolites aimed to identify pathways under tight O₂-dependent control. Finally, we checked the developmental response of kernels grown for extended periods at elevated oxygen concentrations. The combined results were used to mechanistically define the causes and consequences of endogenous hypoxia on growth and metabolism of the developing maize kernel.

Results

Developmental dynamics of kernels is associated with steep gradients of water loss

Following morphogenesis and cellular differentiation (Olsen, 2020), a maize kernel enters the filling phase, in which dry matter deposition is accompanied by decreasing moisture content (Sala et al., 2007). To uncover topological aspects of kernel water dynamics, we here aimed for a detailed picture of water distribution and water loss during the main filling phase. Application of MRI allowed us to selectively

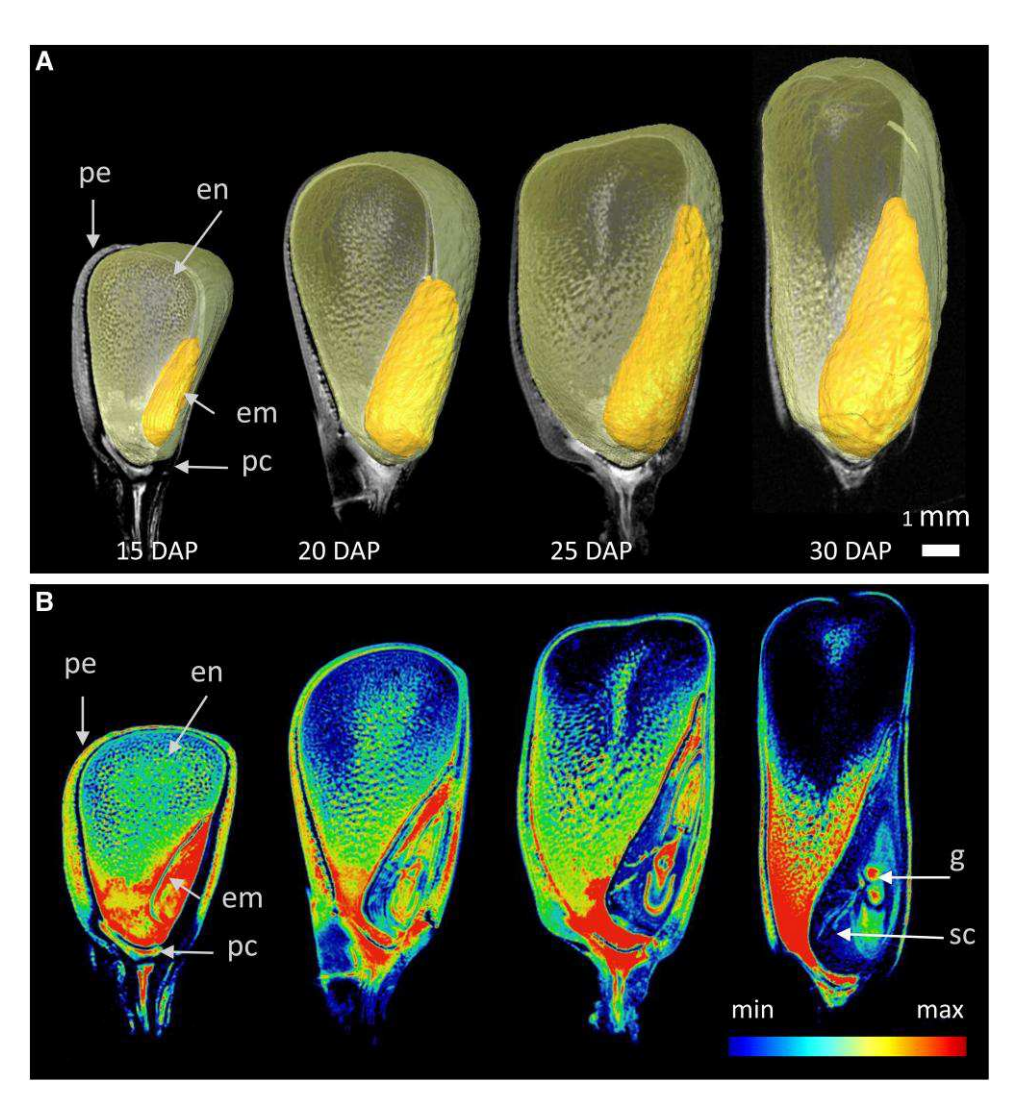


Figure 1 Growth and water distribution in maize kernels during grain-filling stages. A, An MRI-based three-dimensional kernel model showing embryo and endosperm at 15, 20, 25, and 30 DAP; (B) distribution of the water-specific signal (color-coded) in virtual sections (longitudinal sagittals) through the kernels shown in (A) measured by MRI. Shown are representative images of three biological replicates (individual kernels) per stage. Note that all images in (A, B) were digitally extracted for comparison, and use the same scale bar. Abbreviations: pe—pericarp; en—endosperm; em—embryo; pc-pedicel; sc—scutelum; g—germ.

visualize the water distribution across tissues in vivo during development. Based on individual kernel models (Figure 1A), the kernel volume increased from 105 to 245 mm³ between 15 to 30 days after pollination (DAP). At 15 DAP, all tissues of the grain were well-hydrated with the greatest water signal present in the chalazal region and subtending pedicel (Figure 1B). Later in development, water content decreased preferentially in apical regions of the endosperm and basal regions of the embryo. The water loss proceeded during development, forming a steep gradient in local water content. Toward maturity, abundant water remained only in basal zones of the endosperm and central parts of the embryo, whereas apical portions of endosperm and embryo scutellum had already lost most of their water signal (30 DAP, Figure 1B).

The developmental pattern of endosperm hydration was topographically inverse to that of starch. Rapid accumulation

of starch occurred during the grain-fill stage, starting in the upper endosperm and proceeding toward the base (Supplemental Figure S1). Starch appeared to increasingly displace the endosperm water. Notably, the gradients in endosperm (de-) hydration directly affect the local oxygen diffusivity. Data from Arvanitoyannis et al. (1994) revealed an oxygen diffusivity of 15% (starch in water) compared with that in water alone (corresponding to a ~6-fold difference when expressed in gas phase equivalents).

Severe endogenous hypoxia during the grain-filling phase is a universal feature of kernels from modern maize lines to their mutants and wild relatives

Oxygen profiles were characterized for developing kernels of distinct genotypes during their near-linear phase of starch deposition (Tsai et al., 1970). Representative profiles are

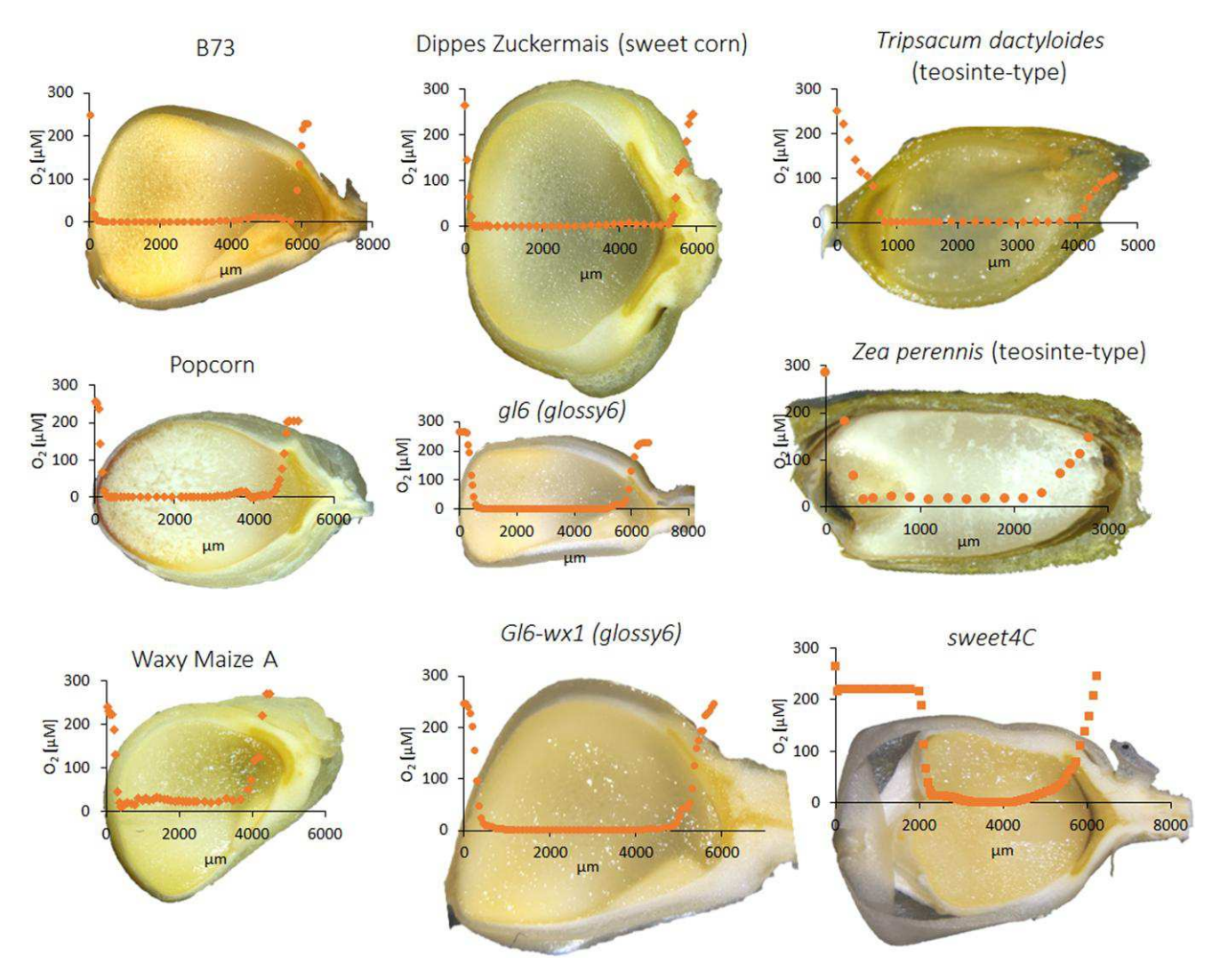


Figure 2 Representative oxygen concentration profiles determined in individual maize kernels (14–20 DAP) of distinct genotypes and non-domesticated wild relatives. Oxygen was measured by microsensors along the x-axis (penetration depth given in μ m). For additional measurements, see Supplemental Figure S2.

shown in Figure 2; additional profiles in Supplemental Figure S2. Across all modern maize genotypes (B73, popcorn, waxy corn, sweet corn), the oxygen level typically dropped dramatically within the first 100-400 µm of the kernel surface, and the remainder of the endosperm showed little detectable oxygen (mean ~3.9 μM, corresponding to 2.86 hPa or 1.38% of atmospheric saturation). Notably, oxygen levels increased strongly, toward the basal endosperm transfer layer, which implies that substantial oxygen entry occurred in the placental chalazal region of the kernel. In the two wild relatives of maize, Z. perennis and Tripsacum dactyloides, the measured oxygen gradients appeared less steep, but mean oxygen levels in the interior were similar to those of modern maize. The two glossy mutants (with decreased epicuticular wax load and increased cuticule permeability; Li et al. 2019) also showed less steep oxygen gradients, reaching a plateau after 400-900 µm of sensor insertion with similar mean of oxygen concentration.

A notable exception was the kernel's oxygen profile in the *sweet4c* mutant. A portion of the mutant kernel interior remained empty due to disturbed endosperm development (Sosso et al., 2015). When the sensor penetrated the outer cuticle/pericarp, the oxygen level remained at almost ambient levels, but dropped dramatically when entering the endosperm. Such a pattern indicates the presence of a diffusion barrier at the surface of the endosperm rather than that of the pericarp.

Oxygen profiling during distinct developmental stages of B73 (Supplemental Figure S3) revealed that the gradient of oxygen from the exterior toward the kernel's center is initially rather shallow (5 DAP) but later gets much steeper. The gradients suggest that hypoxia develops in the small, growing endosperm, but not the nucellus distal to it during early growth. (The endosperm does not fill the kernel interior until 10 to 12 DAP, when it fully displaces the nucellus; see Leroux et al., 2014.) This developmental pattern may

indicate the establishment of a gas diffusion barrier during early development.

Overall, these profiling data let us conclude that (i) endogenous hypoxia is a universal feature of developing kernels from modern maize to its non-domesticated wild relatives, (ii) oxygen diffusion is not hampered by cuticle/pericarp, but rather the internal tissues themselves (endosperm with immediately adjacent layers), and (iii) the placental chalazal region is relevant for oxygen entry into the endosperm.

Chalazal pericarp harbors a highly porous layer with high diffusivity and relevance for oxygen balance in kernels

High-resolution X-ray micro-computed tomography (μ-CT) was used to (1) unravel the existence and features of a void network, and (2) model oxygen diffusivity, as well as steady state oxygen distribution inside the maize kernel. Results are shown for a fully differentiated B73 kernel at ~20 DAP. A porous layer was identified that enveloped the entire base of the kernel. Based on the µ-CT data, we calculated an average porosity (= volume of pore space/volume of whole tissue type) of 34% in a region of the pericarp. This layer did not extend distally up the endosperm side of the kernel but did rise across the face of the developing embryo (Figure 3, A-D, Supplemental Movies S1 and S2). A few small pores were also evident in the embryo and these connected to the porous layer (Supplemental Figure S4). No porous structures were found in endosperm regions of the µ-CT images, indicating that voids were either completely absent or very small (<5 μm). The resulting oxygen diffusivity was calculated for kernel tissues and found to differ by five orders of magnitude (Figure 3E), with highest resistances evident in both the endosperm and non-porous outer pericarp. In addition to diffusivity, localized respiratory activity is a determinant of oxygen distribution. The use of planar oxygen sensors (Supplemental Figure S5) revealed that the embryo has a superior respiratory activity of 2.56-fold (standard deviation 0.72; n = 5) compared with the endosperm.

In the next step, the rendered 3D kernel model (Supplemental Movies S1 and S2) was combined with the respiratory data to compute the internal 3D oxygen distribution. The modeling outcome (Figure 3F) corresponded closely to the microsensor profiling data: the low diffusivity and large size of the endosperm resulted in rapid and complete depletion of oxygen in layers of this tissue extending all the way to those immediately inside the pericarp and embryo. The results indicate that the endosperm itself is a major barrier to oxygen transfer. The establishment of a lipidous layer at the endosperm's surface may additionally increase diffusional resistance. The high diffusivity in porous chalazal pericarp was consistent with the high concentrations of oxygen throughout the embryo despite its higher respiratory demand relative to endosperm. The oxygen model generated here now allows computation of steady state O₂ concentrations across all planes/regions of the kernel as exemplified in Supplemental Figure S6.

The simulation of total mass flow revealed that 43% of all oxygen likely enters the endosperm via direct contact with sites of porous pericarp, whereas only 16% would enter via the non-porous upper surface. For embryos, 41% of their oxygen likely flows from the kernel base, but only 2% of that flow would move further into the endosperm. Different levels of oxygen diffusivity in the outer pericarp were modeled to evaluate whether this layer could contribute a substantial resistance to oxygen diffusion in the maize kernel. Results showed that modest changes in oxygen diffusivity of the outer pericarp did not substantially affect oxygen distribution in the embryo, mainly due to the relatively small size of the embryo and the presence of pores connected to the porous layer. However, when a lower oxygen diffusivity (1× 10⁻¹¹ m² s⁻¹) was modeled to describe the outer pericarp, a sharp decrease in oxygen concentration appeared in the upper endosperm (surrounded by a non-porous region between outer pericarp and endosperm).

To conclude, (1) the peripheral (maternal) void network inside the maize kernel has high relevance for oxygen supply of the basal endosperm and embryo, and (2) the steep oxygen gradients can be purely caused by the very low diffusivity of the endosperm (except basal regions).

Formation of potential gas permeability barriers during kernel development

CT-based modeling demonstrated that diffusion resistance inside the endosperm is very high. Compared to the modeled O₂ concentrations, the measured O₂ gradients at the endosperm periphery appeared even steeper (Supplemental Figure S6B and C). Results thus imply that additional diffusion constraints could be involved. Such restrictions to gas diffusion might be imposed by lipidous layers (Borisjuk and Rolletschek, 2009). We therefore tested for their possible presence and chemical nature in the developing kernel (B73) using localized micro-ATR spectroscopy (Figure 4, A-E). Three characteristic regions were probed, (1) the starchy endosperm, (2) the endosperm surface layer (mainly aleurone), and (3) the outer epidermal layer of the pericarp. The corresponding spectra (Figure 4, C-E) showed association with cutin- and wax-related features in the spectral region of 3600-2800 1/cm. A dominant representation of cutin IR features was evident at the endosperm surface (Figure 4D) as well as the outer epidermal layer of pericarp (Figure 4E). When looking at the infrared fingerprint region (wavenumbers <1800; Supplemental Figure S7), the association of cutin with these tissues was confirmed, since cutin related C = Oand C-O-C vibrations were evident in the representative fingerprint spectra at ~1,730 and 1163 1/cm. As expected, carbohydrate features (around 1100-1000 1/cm) were especially descriptive for the endosperm.

To non-invasively access the appearance of lipidous layers across the entire developing kernel, we next exploited MRI. Due to the different frequencies of proton signals, images from water-only and lipid-only can be acquired along with

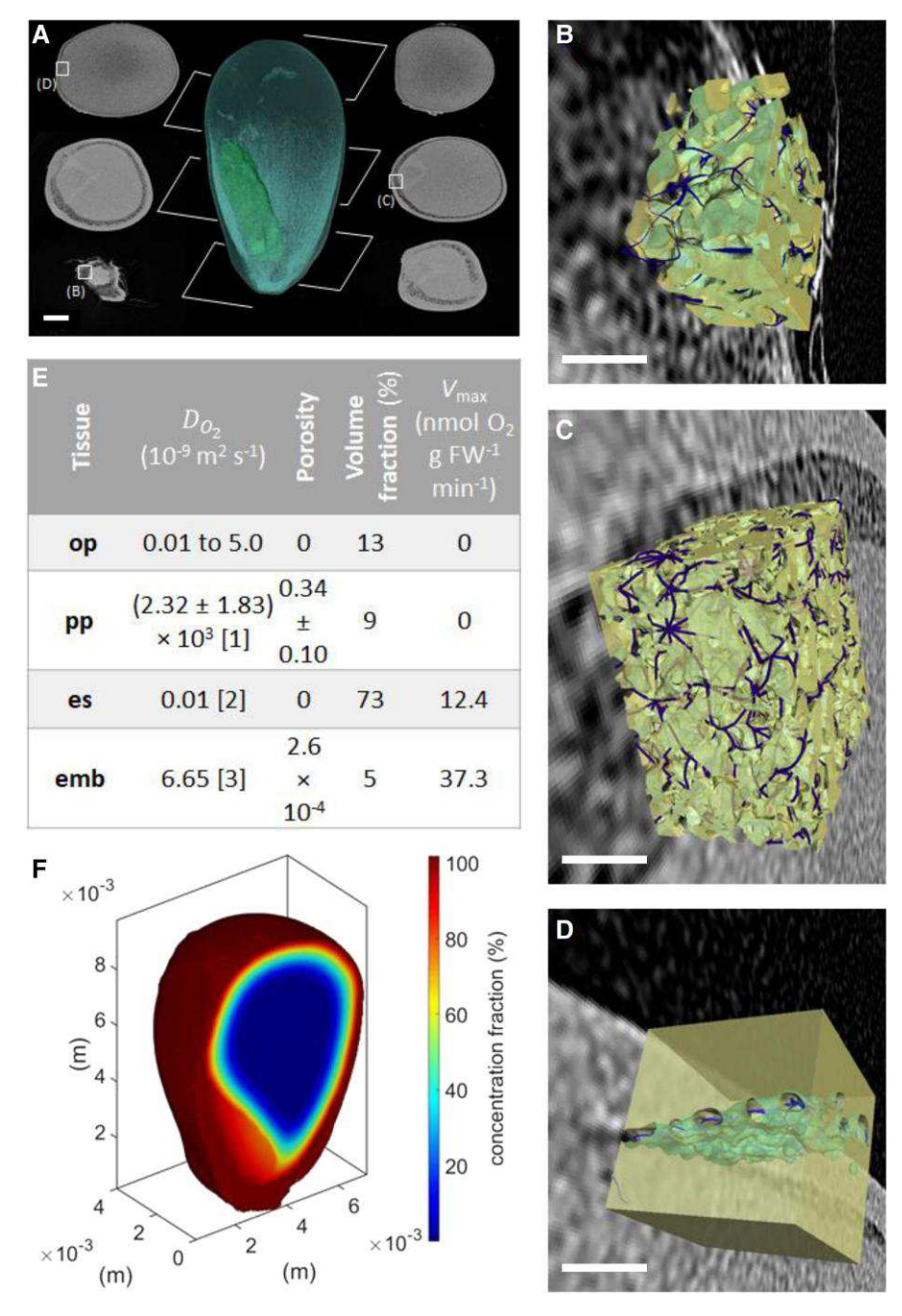


Figure 3 Modeling of kernel void space, oxygen diffusivity, and oxygen distribution. A, μ -CT imaging analysis with a pixel resolution of 5 μ m. The central image is a 3D rendering of the kernel, with the segmented porous layer (blue) and the embryo (green). Subplots are horizontal cross sections through the CT scan at sites progressively further from the kernel base; scale bar = 1000 μ m. Note that all images were digitally extracted for comparison, and use same scale bar. See also Supplemental Movies S1 and S2. (B–D) Rendering of the porous pericarp (in sub-volumes of approximately $50 \times 50 \times 50$ pixels) at different positions indicated by the rectangular boxes in (A), with a well-connected pore network (blue, average porosity = 34%) through tissue (yellow) in the lower part of the kernel, decreasing in width along the height; scale bars = 100 μ m. E, Modeling parameters for distinct maize kernel tissues (emb: embryo, es: endosperm, op: outer pericarp, pp: porous pericarp). [1] Calculated from a microscale oxygen diffusion simulation, n = 6, mean \pm standard deviation; [2] Arvanitoyannis et al., 1994; [3] Estimated by assuming oxygen diffusion in two phases (water and air) based on porosity value. F, Modell of oxygen concentration in a longitudinal plane.

the characterization of seed architecture (Munz et al., 2016). The lipid topology in vivo is shown relative to kernel structure in Figure 4, F–K and Supplemental Movie S3. The 3D model and virtual sections clearly demonstrate that a lipid-rich layer

(storage lipids in aleurone plus wax/cutin-containing layers) completely encloses the endosperm except at its chalazal region (arrowed in Figure 4, G–J). Only the chalazal region of endosperm is thus free of potential gas diffusion barriers.

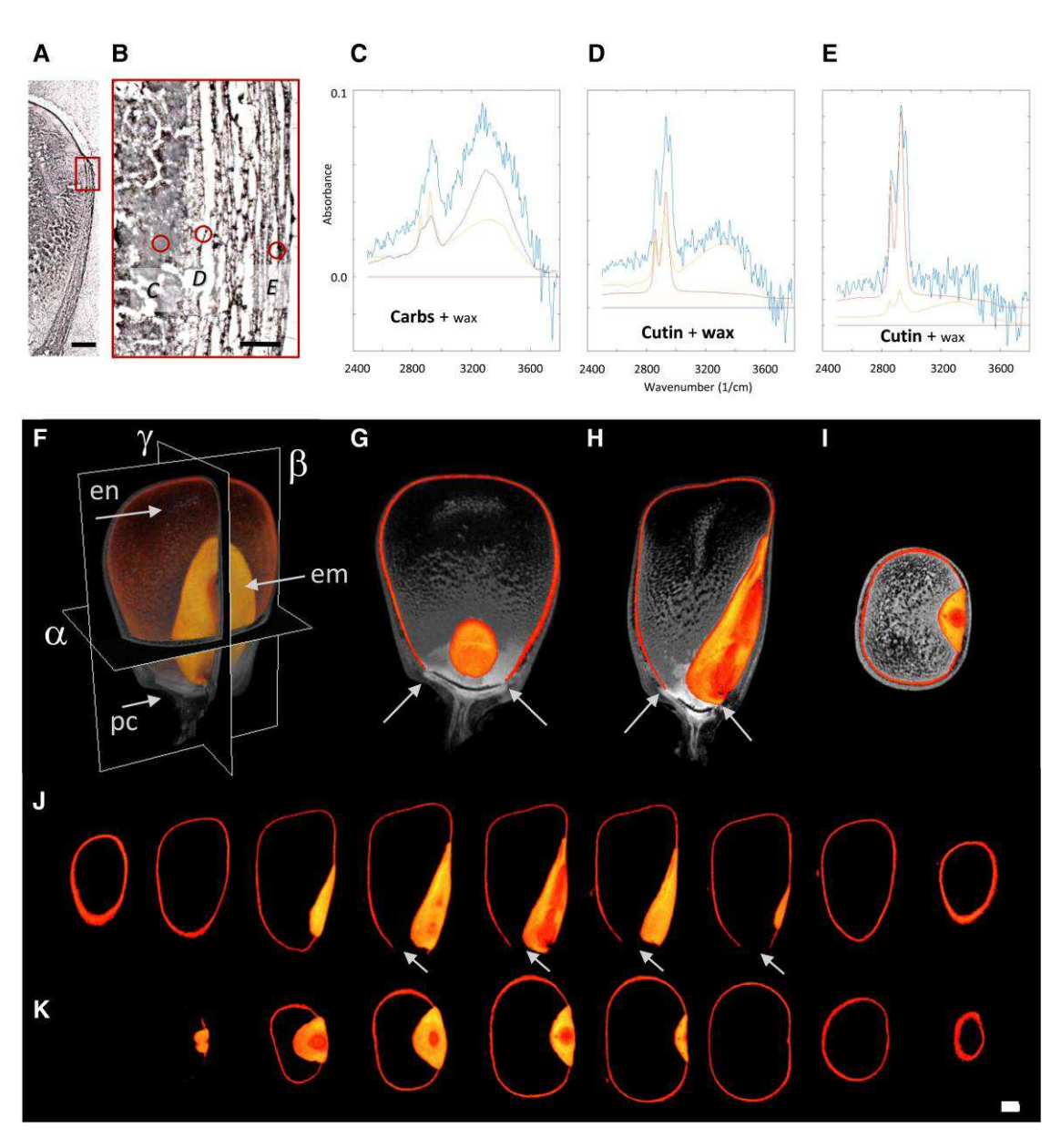


Figure 4 Features of lipidous layers covering the endosperm of developing maize kernels (B73, ~25 DAP). (A–E) Chemometric analysis of micro-ATR image spectra of maize kernels where (A) gives an overview image of a cryo-sectioned maize kernel; a red box locates the analyzed region for ATR imaging; the magnified image in (B) depicts the location of the analyzed spectra (C–E) for starchy endosperm (C), endosperm surface layer (D), and outer epidermis of pericarp (E). Spectral panels in (C–E) present the measured spectrum at the given location in blue, and superimposed contributions of cutin (red), wax (yellow) and carbohydrate (purple, carbohydrate) library spectra. The dominant spectral feature is underlined in bold letters. The micro-ATR data provide the mean of 1,000 spectra (technical replicates) measured at three regions (biological replicates) per tissue type. (F–K) MRI-based lipid mapping indicating the presence of lipid at the endosperm surface and in the embryo. The sample shown in (H) is the same as that in Figure 1 (A–B). F, 3D model and its virtual sections shown in (G–I); arrows indicate the lack of lipidous layers at the basal endosperm region; (J–K) Consecutive virtual sections along the alpha and beta planes shown in (F). Shown are representative images out of three biological replicates (individual kernels). All images in (F–K) were digitally extracted for comparison, and use the same scale bar. See also Supplemental Movie S3. Bars: 500 μm in (A), 100 μm in (B), 1 mm in F–K. Abbreviations: en—endosperm; em—embryo; pc—pedicel.

Key players in the reciprocal molecular adjustment to modulated oxygen availability

To identify molecular adjustments to local oxygen availability, we next treated intact attached kernels with gas mixtures containing either 10, 21, or 30 vol% of oxygen (termed Low- O_2 , Control, and High- O_2 treatments, respectively).

These concentrations were sufficient to reciprocally affect the expression of hypoxia-core genes as verified by RT-qPCR (Supplemental Figure S8).

RNA-sequencing revealed mRNA profiles for kernels sampled after 24 h of Low-O₂, Control, and High-O₂ treatments. High-O₂ had modest effects, significantly altering

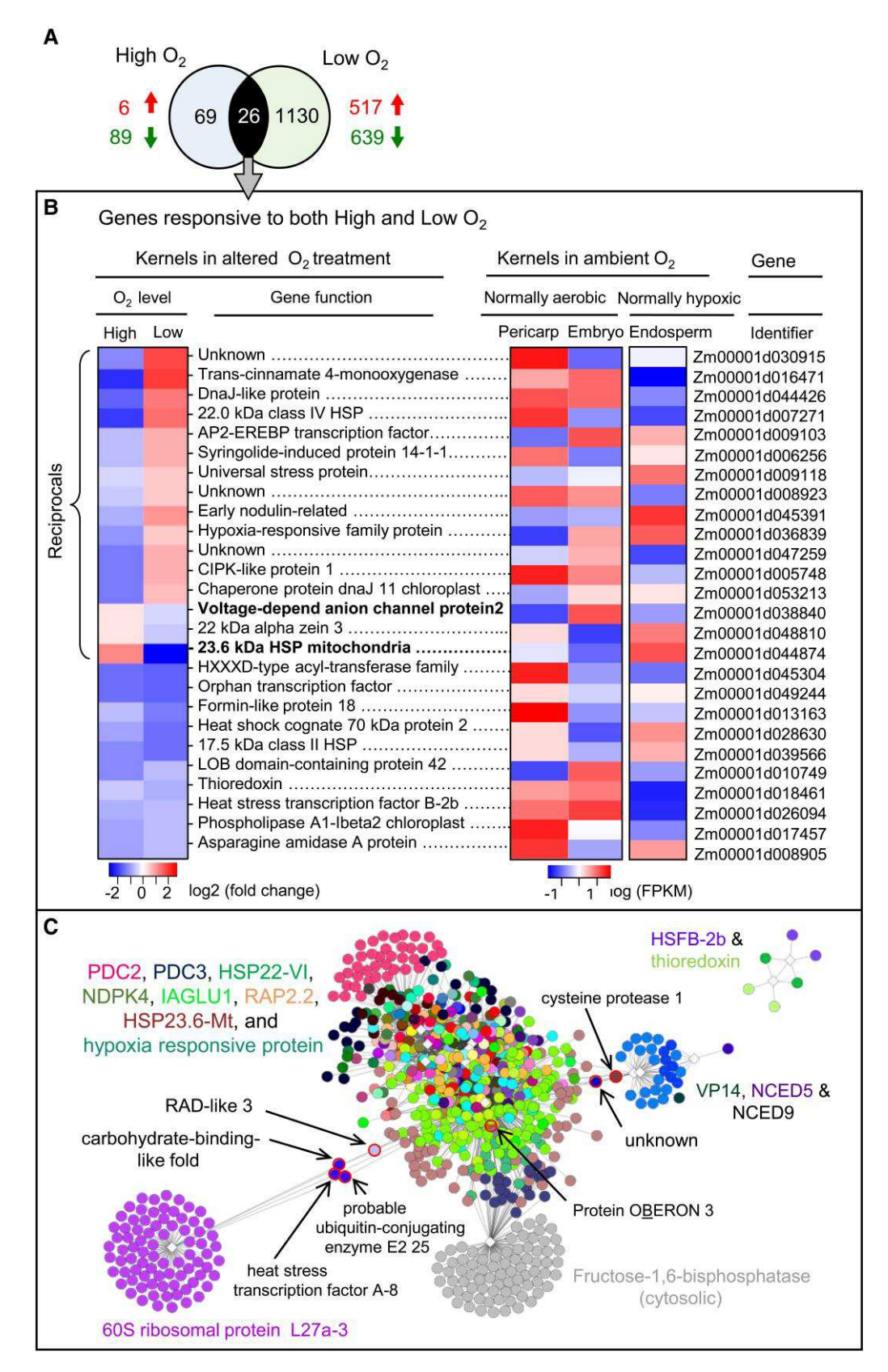


Figure 5 Regulation of kernel transcriptome profiles and gene-network responses by oxygen availability (B73, 18 DAP). RNA was extracted from maize kernels at 18 DAP (five biological replicates each consisting of three individual kernels). A, Venn diagram of differentially expressed genes (DEGs) unique to- or shared between Low- and High-oxygen treatments (Low- $O_2 = 10$ vol%, High- $O_2 = 30$ vol%, ambient control = 21vol%).

only 95 transcripts (FDR < 0.01), 86 of which were downregulated (Figure 5A and Supplemental Dataset S1A). Low-O2, however, impacted ten-fold more DEGs (Figure 5A and Supplemental Dataset S1B). A group of only 26 genes responded to both High- and Low-O2, with 16 of these DEGs showing reciprocal patterns of expression (upregulated under one condition, and downregulated under the other) (Figure 5B). By lowering the statistical confidence (FDR < 0.05), 15 additional genes were found to show reciprocal responses (Supplemental Dataset S1C). More than half of these 16 high-confidence reciprocally expressed genes were characteristic of stress responses. In addition, most of these genes were not ubiquitously expressed throughout the kernel, but appeared preferentially in either oxygenated tissues (pericarp and embryo) or hypoxic endosperm (Figure 5B and data on 13 DAP kernels from Doll et al., 2020). Two of these reciprocal-response genes encoded proteins targeted to mitochondria: the regulatory transporter, Voltage-Dependent Anion Channel 2 (VDAC2; Kanwar et al., 2020) and the master modulator of electron transport, 23.6-kDa Heat-Shock Protein (HSP23.6; Ma et al., 2019). The latter showed the strongest downregulation and was normally (grown at ambient levels) most abundant in the endosperm.

To investigate the relationship between oxygen-responsive transcripts and their sites of expression, we compared the most prominently impacted mRNAs to their distribution in transcriptomes of tissues from ambient-air kernels at 13 DAP (Supplemental Figures S9 and S10 with additional data from Doll et al, 2020). Under High-O₂, the most prominently downregulated DEGs were ones otherwise expressed at diverse sites in kernels growing under ambient oxygen. The upregulated genes, however, predominated in the embryo of ambient-air kernels. In contrast, Low-O₂ strongly upregulated genes normally expressed in the pericarp, whereas those downregulated often predominated in endosperm of ambient-air kernels. A closer look at genes downregulated by High-O₂ showed that roles of many were implicated in oxidative stress and were most often expressed in pericarp

of ambient-air kernels (Supplemental Figure S11). Further comparison of these transcriptomes showed that many genes responsive to High-O₂ were categorized as temperature sensitive (including HSPs with diverse functions). Interestingly, this functional category was also prominent among genes upregulated by Low-O₂ and in endosperm of ambient-air kernels (Supplemental Figure S10 with Doll et al., 2020). Low-O₂ upregulated genes related to ABA (9-cis-epoxycarotenoid dioxygenase3 (NCED3) and viviparous14) and alcohol responses but downregulated others for assembly and organization of nucleosomes and peptide biosynthesis (Supplemental Figure S12).

Gene expression networks responsive to high and low O₂ conditions

We next sought deeper insights into potential functional and regulatory relationships among the 1,222 genes responding to oxygen perturbation. To do so, we selected 15 with known roles in other systems to use as probes for defining coexpression networks (Figure 5C and Supplemental Dataset S2). Since genes with similar functions tend to cluster together, this approach allowed an outline of possible commonalities in roles and regulation. Five co-expression modules emerged (Figure 5C) indicating involvement of at least five regulatory mechanisms. Among these modules, was a large cluster that included eight bait genes along with other mRNAs central to respiration, stress responses, and biogenesis of cellular components. Three of the other modules were distinct from but related to this large cluster. One was defined by the ribosomal L27a-3 bait and included other nucleosome- and ribosome-related mRNAs, consistent with the extent of restructuring in response to treatments. The second module included the two bait genes, viviparous14 and NCED5, as well as NCED9, collectively indicating a level of coordinate expression between the major respiratory cluster and genes encoding biosynthesis and sensing systems for ABA. A third module defined a separate source of respiratory input, yet one closely coordinated with the

Figure 5 (Continued)

Total DEGs responding to one or both treatments are shown inside the Venn diagram, with upregulated DEGs alongside in red and downregulated DEGs in green. Expanded analysis of the 26 genes responsive to both high and low O₂ appears below (gray arrow). B, Expression (log2-fold change) of the 26 DEGs responding to both High- and Low-O₂ (left column), together with their annotation (left center), expression in tissues of ambient-air grown kernels at 13 DAP (right center) (RNA-seq data from Doll et al., 2020), and gene identifiers (right column). Two genes of particular interest are shown in bold, the HSP23.6 (master regulator of mitochondrial electron transport), and the Voltage-dependent anion channel protein 2 (VDAC2; mitochondrial regulatory transporter). C, Gene expression networks for key responses to oxygen availability in maize kernels. Networks and their relationships were defined from among 1,222 genes that responded to oxygen perturbation (see Supplemental Datasets S1D and S1E) by using 15 bait genes selected from this group based on their known roles in other systems. Co-expressed modules were identified in transcriptome data from 14 different RNA-Seq libraries constructed and sequenced here, each representing responses of 18-DAP maize kernels under either control (21% O2 v/v), low (10% O2 v/v) or high-oxygen conditions (30% O2 v/v) using CoExpNetViz (Tzfadia et al., 2015). Data were analyzed using the Pearson correlation co-efficient, with the 5 lowest and 95 uppermost percentile rankings as thresholds for co-expression. Bait gene abbreviations are shown in colored text near the modules they define (full names, annotations, gene identifiers, and color coding are as in Supplemental Dataset S2). Dots with the same color represent genes co-expressed with a given bait based on positive correlations where R2 > 0.8. Five genes with high betweenness scores (hub nodes) indicative of essential points of connection are highlighted with a red outline and their corresponding genes are labeled in black (see als

main cluster. This one was delineated by a gene for the glycolytic enzyme, cytosolic fructose-1,6-biphosphatase (F-1,6 BPase) and transcripts for mitochondrial membrane proteins. This group of coordinately expressed mRNAs is consistent with evidence for a functional association between F-1,6 BPase and the mitochondrial membrane protein VDAC2 (Voltage-dependent anion channel 2) (Gizak et al, 2019) as well as a moonlighting role for this protein as a transcriptional regulator in other systems (Cho and Yoo, 2011; Gizak et al., 2019). Analyses here also indicate that the thioredoxin and HSFB-2b module was probably regulated independently of the others. A notable result was the extent of co-expression observed for VDAC2, which closely paralleled that of six bait genes (HSP22.0-IV, sHSP23.6-Mt, Hypoxia-responsive protein, PDC3, NDPK4 and RPL29). In other systems, the VDAC2 occupies a pivotal role in regulating metabolite transfer between cytosol and mitochondria (Kanwar et al., 2020). Still another finding was the identification of seven genes with betweenness-centrality scores that indicate essential links between clusters, often with regulatory roles (Figure 5C and Supplemental Dataset S2). Five of these genes were implicated in control of signaling or transcription. Lastly, we were especially interested in the degree to which the large respiratory module shown here was interconnected with genes showing reciprocal expression (both up and down regulation) across the range of oxygen treatments. Each of these genes thus provides a point of interface between the major respiratory module and kernel adjustment to the full spectrum of oxygen perturbations tested here.

Energy, sugar, and auxin metabolism instantly respond to modulations in oxygen availability

To test the temporal dynamics of the kernel's metabolome in response to oxygen supply, we used kernels treated as above, and sampled at 0.5, 1, 2, 4, 12, and 24 h after the start of treatments. Untargeted metabolite profiling allowed identification and quantification of 125 metabolic intermediates covering the major pathways of central metabolism as well as auxins (Figure 6 and Supplemental Dataset S3). Major trends seen in responses to the Low-O₂ treatment were a reduction in sucrose-6-P levels (precursor for sucrose resynthesis) and accumulation of diverse intermediates. The latter included (i) ADP-glucose (precursor for starch synthesis), (ii) IAA-Asp (degradation product of IAA), (iii) intermediates of lower glycolysis (most evident for pyruvate), (iv) allantoin and allantoate (degradation products of urate), (v) panthothenate (relevant for synthesis of coenzyme A used for the TCA cycle and elsewhere), (vi) ribonate (sugar acid from the pentose-P pathway), and finally (vii) up to fivefold increases in 2-oxoglutarate, GABA, and 4-hydroxybutyrate (fermentation product). The latter is indicative of some GABA-shunt activity, which is however redirected from its normal return to the TCA cycle to instead, formation of 4-hydroxybutyrate (Shelp et al., 2017). Despite an induction of ADH1 expression, Low-O2 treatment did not lead to an accumulation of the classical fermentation products (ethanol, alanine or lactate). A possible avoidance strategy was considered and is consistent with the transient, but strong increase in caprylate at 30 min of treatment. This compound (also known as octanoic acid) is a fermentation inhibitor in yeast (Licek et al., 2020). Some of the intermediates mentioned above showed strongly reciprocal behavior under Low-O₂ vs. High-O₂. Among these were ADP-glucose, IAA-Asp, and GABA.

In contrast to Low- O_2 treatments, major trends in responses to High- O_2 included the almost complete loss of ascorbate (major antioxidant) toward end of treatment. This decrease indicated that antioxidant capacity was strongly compromised after 12 to 24 h of elevated oxygen. We further noted lower levels of ADP-glucose and IAA-Asp, as well as intermediates of lower glycolysis (3PGA and PEP), and some organic acids (malate and succinate).

Unexpectedly, lowered abundance of all four nucleotide tri-phosphates was noted in data from both High-O₂ and Low-O₂ relative to control treatments. This change in abundance of NTPs was sometimes accompanied by (transient) increases in mono- and di-phosphorylated nucleotides, pointing to some mechanism of energetic balancing.

Elevated oxygen supply over long-term causes a progression in kernel development

To check for developmental adjustments of kernels to elevated oxygen supply, we used a standardized in vitro approach (Gengenbach & Jones, 1994) with 17 days of cultivation under either High-O₂ (30 vol%) or control conditions (21 vol%). High-O₂ caused a visible phenotype: a more progressed development (Supplemental Figure S13). MRI-based imaging of representative kernels revealed that High-O₂ led to a substantially lower water signal in both upper and central endosperm regions as well as in the embryo scutellum (Figure 7A). This finding corresponded to lowered water content of entire kernels determined gravimetrically (Figure 7B). While dry weight of kernels did not show statistically significant effects of treatment (Figure 7C), we noticed that High-O2 resulted in a proportional increase of both fresh and dry weights of embryo versus endosperm (Figure 7E). This shift in dry matter accumulation also corresponded to the higher ¹³C/¹⁵N-label abundance measured in embryo under High-O2 vs. Control conditions, following feeding with labeled sugars/amino acids (Figure 7F). Total label uptake of kernels was, however, not affected. Regarding biomass composition, the most notable response to High-O₂ was the greater level of starch in endosperm (21% versus 14% of fresh weight; compensated by lower water content) (Figure 7D). Treatment effects on steady state metabolite abundance were minor (Supplemental Figure S14; Supplemental Dataset S4). The largest increase resulting from High-O₂ was that of fumarate, and the most prominent decrease was in isocitrate (both representing TCA cycle intermediates). Altogether, we conclude that long-term

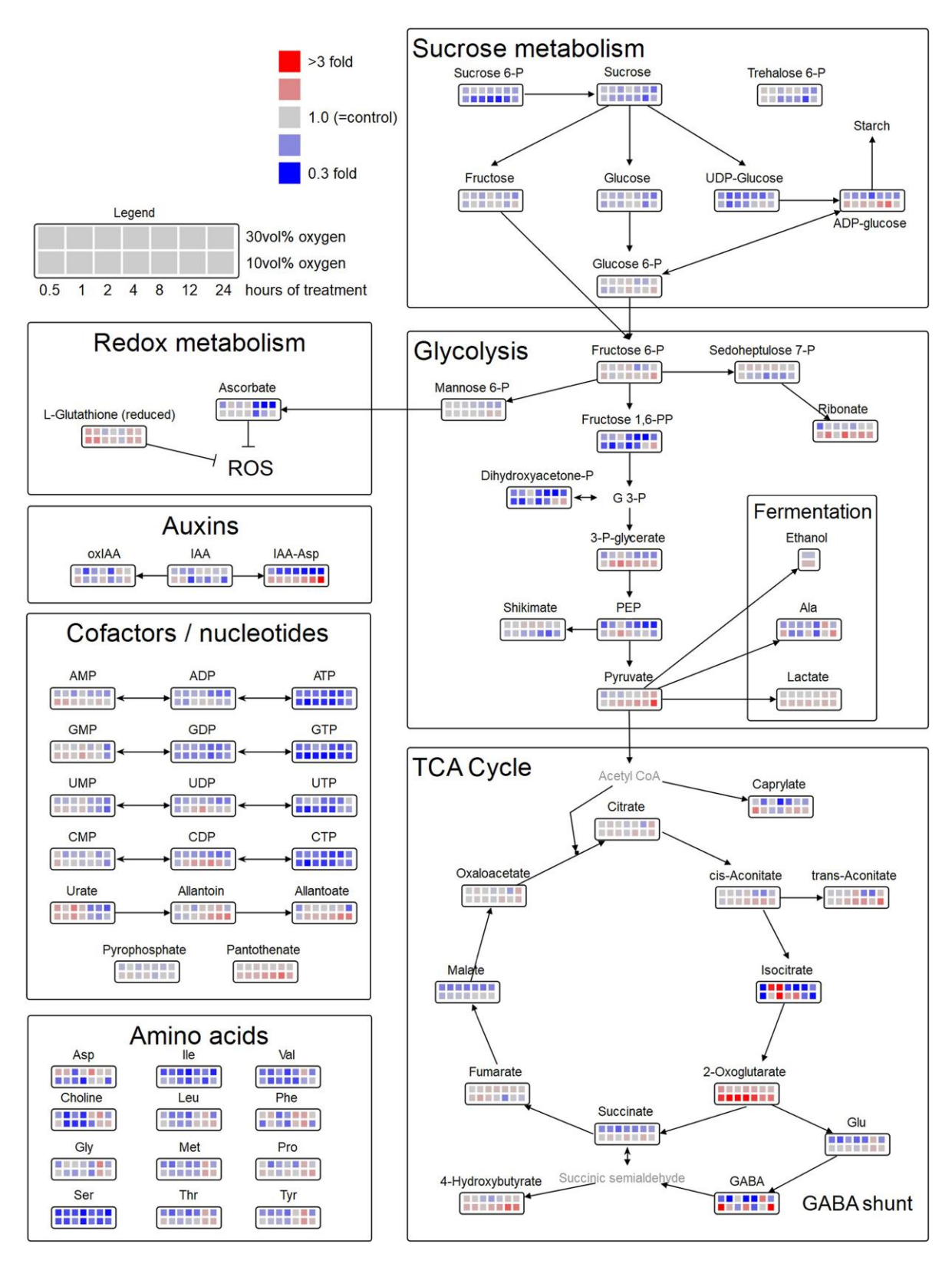


Figure 6 Metabolite heat map illustrating the abundance of selected intermediates in the developing kernel in response to High- O_2 and Low- O_2 treatment (30 and 10 vol%, respectively). B73 kernels were sampled at distinct time intervals and measured using LC/MS (n = 5, each sample consisting of three kernels). Ethanol was measured after 24 h of treatment using a photometric assay. Data are given relative to those of controls (21 vol%). All details are given in Supplemental Dataset S3.

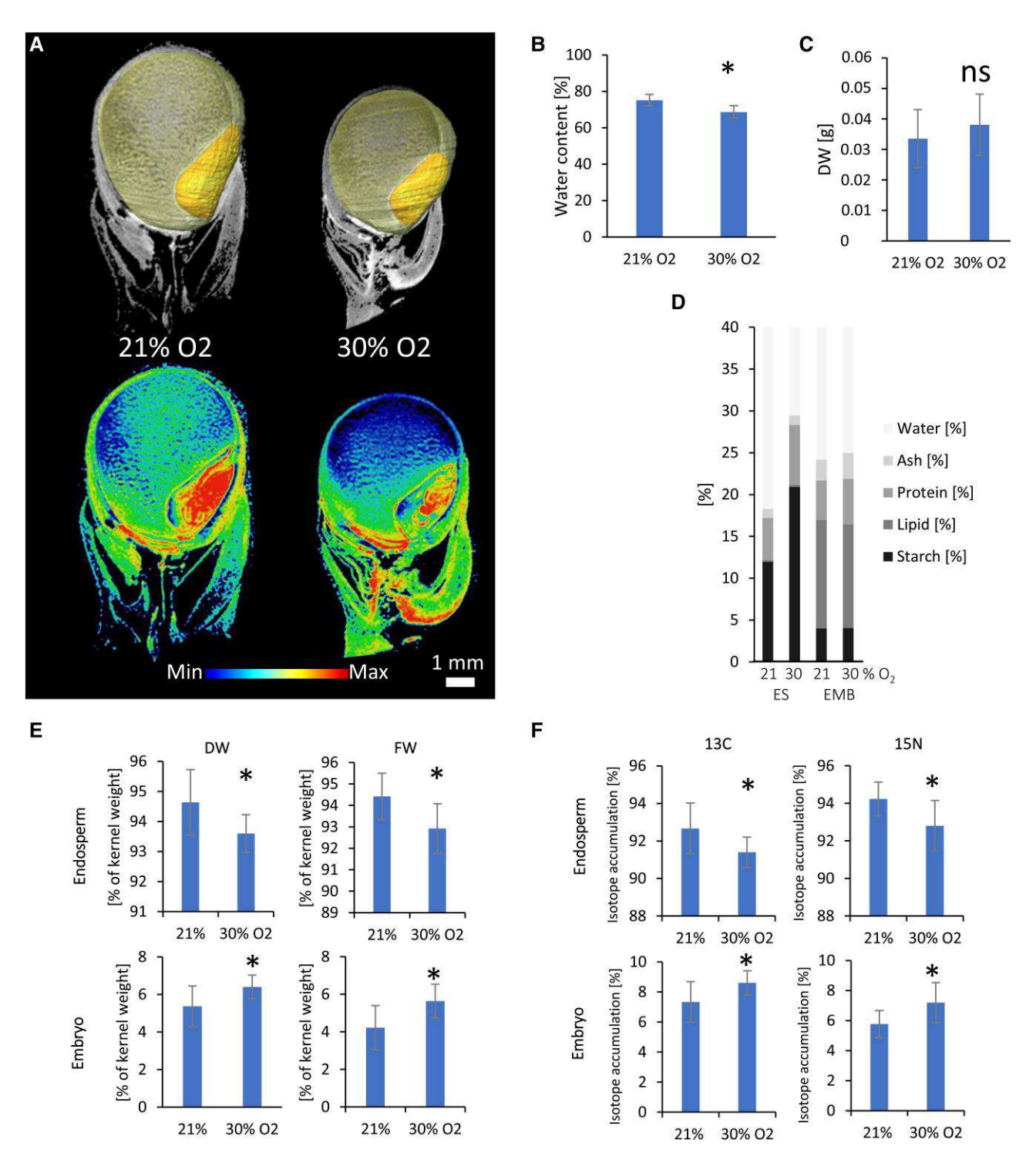


Figure 7 Long-term effects of elevated oxygen supply on kernel growth. Kernels were cultivated in vitro from 10 to 27 days after pollination under either control (21 vol% of oxygen) or High- O_2 conditions (30 vol%). A, An MRI-based three-dimensional model showing embryo and endosperm (upper panel) and distribution of the water-specific signal (color-coded) in virtual cross sections through these kernels (lower panel). All images were digitally extracted for comparison, and use the same scale bar and color code. (B and C) Gravimetric analysis of water content (B) and dry weight (C) of kernels. D, Biomass fractionation for endosperm (ES) and embryo (EMB); please note that y-axis is set to 40%. E, Fresh and dry weight of separated endosperm and embryo fractions. F, Abundance of ¹³C and ¹⁵N isotopes in separated endosperm and embryo fractions following feeding with labeled sugars/amino acids. Data in B-F are means \pm standard deviation (n = 8–10 individual kernels). * indicates statistical significance according to t-test (P < 0.05); ns = not significantly different.

elevations in oxygen supply enhance progression of kernel development, which includes a shift in assimilate partitioning favoring embryo growth.

Discussion

Structural features shaping oxygen dynamics in the developing maize kernel

Respiration is generally the major sink for oxygen in plant tissues. How then does the intensely respiring embryo avoid oxygen depletion, while hypoxia develops in the endosperm? The reason includes prominent impacts of structural elements of the kernel and their physical parameters, which either constrain or accelerate gas diffusion and therewith control oxygen supply and are summarized in Movie 1. We identified the following core elements: (i) A previously unknown but well-developed void space is present in the basal region of maize kernels (Figure 3). Analysis of this porous layer by μ -CT and further modeling clearly revealed its high diffusivity and quantified its relevance for the overall oxygen balance. (ii) Although the outer cuticula of the pericarp was expected to be the relevant barrier to gas exchange, oxygen profiling and modeling revealed instead, that the endosperm itself constitutes a major limitation to diffusion (Figure 2). (iii) A potential barrier identified here is a lipidous layer found to enclose the entire endosperm except at the placental chalazal region (Figure 4). These epidermal (aleurone) cells are known to accumulate storage lipids but are apparently tightly associated with layers of cutin and wax (Figure 4, D and E). Such lipid polyesters are known for their capacity to form a protective barrier that hampers gas diffusion (Lendzian, 1982; Borisjuk & Rolletschek, 2009). The progressive crushing of nucellar cells (and inner integument) could have contributed some or all of this barrier material (Johann, 1942; Leroux et al., 2014). The rapid onset of this stage in nucellar maturation and its programed cell death also corresponds to enhanced kernel size and starch storage (Sun et al., 2022). The impact of this layer is further supported by oxygen profiling during early growth phases (Supplemental Figure S3), which indicated a barrier at the endosperm-nucellus interface. Please note that lipidous layers are not just a potential barrier to gas exchange but can act as barrier to water movements (thereby restricting uncontrolled water loss). Finally (iv), gradients in water and starch content form during late stages of endosperm development and inevitably induce gradients in oxygen solubility and diffusivity. High local starch content (displacing water) therefore contributes to steep O₂ concentration gradients in endosperm.

The well-hydrated chalazal endosperm remains well oxygenated via the porous basal layer (void network) throughout the grain-filling phase. The basal endosperm transfer layer (mediating assimilate transfer into endosperm; Chourey & Hueros, 2017) is therefore not exposed to the endogenous hypoxia nearby. This conclusion is not only based on oxygen

profiling/modeling data (Figures 2 and 3) but also implied by evidence that the more rapid rate of kernel development at, High-O₂ levels was not accompanied by increased assimilate import (Figure 7).

Key components of metabolic acclimation to hypoxia Hypoxia in the developing maize endosperm is a standard state, being established from early stages onwards (Supplemental Figure S3). This constancy of normal hypoxia poses a challenge for assessing whether components of normal endosperm development (fluxes, expressed genes, etc.) actually represent adjustments to hypoxia or not. The experimental modulation of oxygen supply to the kernel, as applied here, aimed to identify regulatory and metabolic elements associated with acclimation to hypoxia.

Potential keys to oxygen regulation of kernel metabolism were revealed by the genes identified here that showed reciprocal responsiveness (Figure 5B and Supplemental Data Set S1C). The importance of these observations lies in their implication of roles for sensing and/or adjusting to changes in localized oxygen availability. Among these genes is one encoding a VDAC2 and another for an HSP23.6, both upregulated by oxygen abundance and targeted to mitochondria. The VDAC2 is a central regulator of mitochondrial function, controlling the metabolite trafficking between mitochondria and cytosol, and partnering with glycolytic enzymes like F-1,6BPase (Kanwar et al., 2020). The VDACs can also regulate mitochondrial Ca2+ homoeostasis, and transport reactive oxygen species (ROS) from mitochondria to the cytosol. The HSP23.6 has a role in control of the electron transport chain and respiratory activity (Ma et al., 2019). Network relationships with the HSP23.6 indicated that its regulation was closely associated with that of other low-oxygen-responsive genes (Figure 5C). In the maize kernel, both VDAC2 and HSP23.6 likely function in balancing mitochondrial activity, thereby contributing to not just metabolic acclimation, but also mitochondrial functions as sensors of stress and signaling hubs (Meng et al., 2020).

The prime importance of mitochondrial adjustments is further seen by substantial shifts of GABA-shunt intermediates upon low-oxygen treatment. Rising levels of oxoglutarate and GABA are consistent with GABA-shunt activity, but an open loop is indicated in the present instance by their accumulation together with that of 4-hydroxybutyrate. Accumulation of this compound has been observed also in other systems (Shelp et al., 2017), and likely results from the induction of 4-hydroxybutyrate dehydrogenase upon hypoxia (Breitkreuz et al., 2003). This would be accompanied with provision of NAD(P) needed for accelerated glycolysis (relevant under hypoxia). An incomplete GABA-shunt provides a means of redox (NAD/NADH) balancing, and 4-hydroxybutyrate functions in oxidative stress tolerance. Genes relating to the GABA-shunt or TCA cycle were not responsive to the elevated oxygen treatment, nor were those encoding enzymes of glycolysis, gluconeogenesis, or sucrose metabolism (while the intermediates sucrose-6-P and pyruvate were responsive). We conclude that in the maize kernel, most regulation of these pathways appears to be post-transcriptional. This scenario differs from that of transient hypoxia in maize roots (Sanclemente et al., 2021), but is consistent with previous suggestions that respiration and other central metabolic pathways are controlled to a great degree at the post-transcriptional level (Plaxton & Podesta, 2006; Schwender et al., 2014; Hackett et al., 2016).

The Low-O₂ treatment applied here failed to induce accumulation of standard fermentation products (Figure 6), though transcriptional upregulation was evident for alcohol dehydrogenase (Supplemental Figure S8). An avoidance mechanism may be operating, and the transient accumulation of caprylate could be part of it. In other systems, caprylate produced as a by-product in hypoxic conditions is considered a fermentation inhibitor (reducing the formation of the toxic intermediate acetaldehyde; Licek et al., 2020). Although speculative, the early transient rise in caprylate could present a signal, blocking the onset of ethanolic fermentation activity in the kernel. Caprylate and other shortchain acids could also act as enhancers of ethylene action (Friedman et al., 2003), which in turn is a core component of the hypoxic plant response. Redox modifications of alcohol dehydrogenase proteins (Dumont et al., 2018) could contribute to alternative means of avoidance.

High-O₂ had a modest impact on the number of responsive genes, but caused a more rapid rate of kernel development, as evidenced by progressive desiccation (Figure 7). The most prominently downregulated gene under High-O₂ was a BAX inhibitor-1. In Arabidopsis, this gene suppresses programed cell death (PCD) (Watanabe and Lam, 2008). The downregulation of this inhibitor in maize kernels could thus lead to an earlier onset of PCD, a characteristic feature of maturing endosperm. Another marker of more rapid kernel development under High-O2 was the upregulation of an α -zein 3 storage protein typically expressed during late stages of maturation (Stelpflug et al, 2016). Oxygen treatment caused a reciprocal-response for the gene encoding ADP-glucose pyrophosphorylase (upregulation at High-O₂), as well as for ADP-glucose. Given that ADP-glucose synthesis is rate limiting for starch synthesis in maize (Hannah and Boehlein, 2017), our findings imply an elevated synthesis rate for starch at High-O₂. This was also detectable under long-term conditions (Figure 7D).

Hypoxia signaling elements operating in the maize kernel

Oxygen responsiveness was demonstrated here for key elements controlling the oxygen-dependent branch of the N-end-rule pathway. These included RAP2.2 and Plant cysteine oxidase 1. The latter protein appears kinetically tailored to act as an oxygen sensor (White et al., 2018). In addition, other candidate signaling genes were evident, such as guanylyl cyclase 1 (induced under low oxygen). The encoded enzyme generates the second messenger, cyclic GMP, providing a link to myriads of signaling opportunities including plant hormones, phosphodiesterases, protein kinases,

Ca²⁺ and nitric oxide (Duszyn et al., 2019). Cyclic GMP can also bind to ion channels with predicted oxygen-sensing capacity (Wang et al., 2017).

At the hormonal level, we observed an induction of 1-aminocyclopropane-1-carboxylate oxidase15 under low oxygen, and thereby a potential induction of ethylene synthesis. Auxin metabolism was clearly affected. The conjugate IAA-Asp, destined for catabolic metabolism, showed a strong reciprocal responsiveness (Figure 6). Auxin turnover can be very rapid (~10 min; Fukui et al., 2022), and auxin-conjugating enzymes are known to link growth regulation with stress adaptation (Park et al., 2007). In maize kernels, low-oxygen-induced IAA degradation was accompanied by transcriptional downregulation of SMALL AUXIN UP RNA55 (SAUR55), localized to mitochondria. The SAUR proteins provide a functional link to Ca²⁺ signaling, which is integral to hypoxia signaling. Potential effects include auxin-induced cell expansion, cell cycle, transcription of zein coding genes, and others (Bernardi et al., 2019). Neither abscisic acid (ABA) nor its intermediates could be detected in the maize kernel, and other indications on ABA metabolism were rather indirect. Allantoin and allantoate, presumably from urate (nucleotide) degradation, accumulated at Low-O₂ as did transcript levels for NCED3 and viviparous14. Allantoin has been implicated in the induction of NCED3 and subsequent rises in ABA levels (Watanabe et al., 2014). However, oxygen availability could still limit ABA synthesis due to the role of O_2 as substrate in the dioxygenase reactions of NCEDs. Alternatively, allantoin and allantoate could also result from nucleotide salvage accompanying the mRNA turnover during transcriptional reprograming.

Reactive oxygen species are another class of oxygen signaling elements. A surplus of oxygen was previously shown to raise respiratory activity of maize kernels (Rolletschek et al., 2005), and thereby the inevitable production of mitochondrial ROS. Although ROS levels in kernels have not been studied here, High- O_2 treatment completely exhausted the ascorbate pool within hours, a response indicative of elevated oxidative stress. The upregulation of HSP23.6 under High- O_2 is consistent with oxidative stress, since this protein causes a decrease in cytochrome oxidase activity but aids increase in the alternative oxidase pathway (Ma et al., 2019). Such redirection of flux would decrease mitochondrial ROS production to some extent.

Collectively, the importance of our findings are four-fold: (1) we demonstrate that severe hypoxia is the standard state for endosperm in modern maize and its non-domesticated wild relatives, (2) we show the 'where, when and why' of hypoxia establishment in endosperm, and (3) uncover the molecular and biochemical mechanisms associated with acclimation to and maintenance of hypoxia (Figure 8). Finally (4), we demonstrate that oxygen supply takes effect on the kernel's developmental progression. In other words, hypoxia slows down the development of the maize kernel and this needs to be further investigated.

In addition, the data set presented here provides opportunities for further research. For example, the 3D kernel

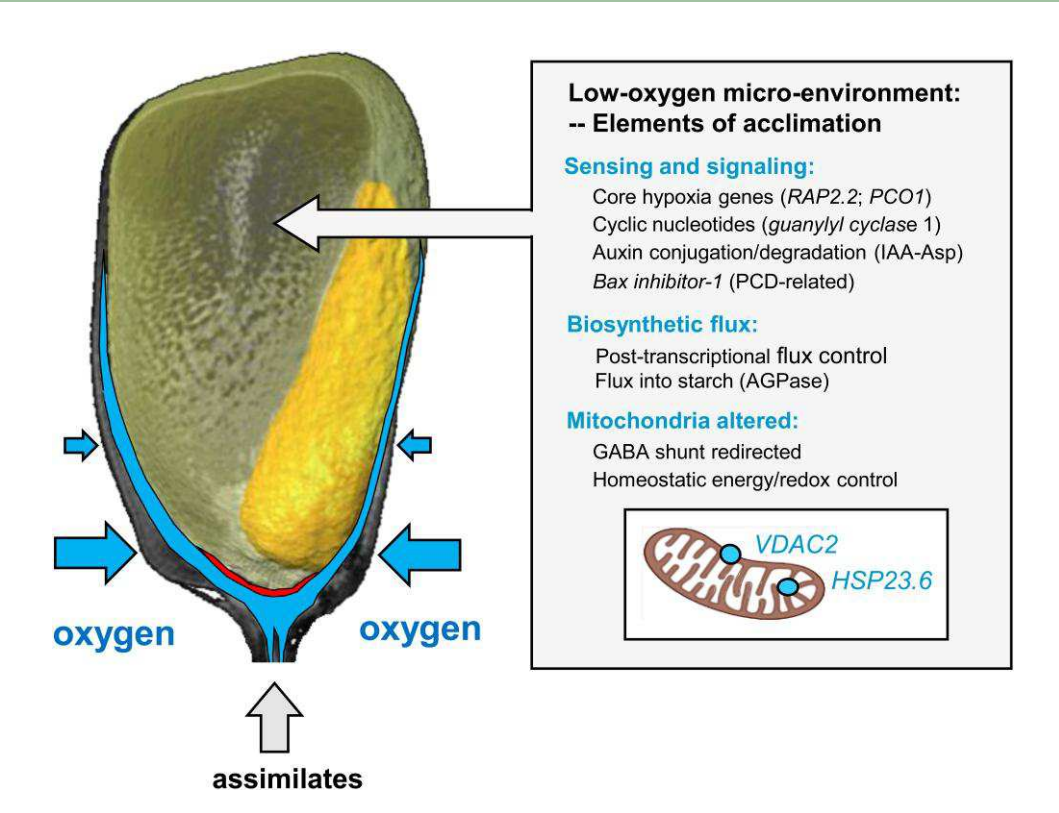


Figure 8 Schematic representation of systems for oxygen and sugar delivery during grain-fill in maize, and core elements for hypoxic acclimation. Left panel: A void space network (in blue) provides a path for oxygen movement to BETL (red) and embryo (yellow) allowing fully aerobic metabolism at these localized sites. The void space includes hydrated cell walls and other portions of the assimilate transport path. In contrast, oxygen supply to most of the endosperm is constrained by its low gas diffusivity and additional diffusion barriers covering the endosperm. Right panel: Local oxygen status in the endosperm is sensed, signaled, and adjusted by reciprocally responsive elements, alterations to biosynthetic pathways, and altered roles of mitochondria. Key players implicated in respiratory control are a VDAC2 regulatory transporter and a HSP23.6 master modulator of electron transport. Abbreviations: AGPase (ADP-glucose pyrophosphorylase); GABA (4-aminobutyrate); HSP23.6 (23.6-kDa Heat-Shock Protein); IAA-Asp (indole-3-acetyl-aspartate); PCD (programed cell death); PCO1 (Plant cysteine oxidase 1); RAP2.2 (RELATED TO APETALA2.2); VDAC2 (Voltage-Dependent Anion Channel 2).

models and the respective water maps (Figure 1) can be employed for understanding the maturation program, sinksource relations, and establishment of desiccation tolerance. Water loss is recognized as a general marker for maize kernel development (Sala et al., 2007), but the hydration/dehydration pattern of kernel tissues are an untapped resource. We show that tissue dehydration is a gradual process, which already starts during early grain filling, and occurs in an organ- and tissue-specific manner. The local onset of storage product deposition in apical endosperm is one obvious reason (as it inevitably reduces the portion of water per total tissue volume); in addition, cell size and other features might also play a role. The 3D models and water maps could be used to analyze fluid transfer capabilities, surface areas, volumes, and the proposed tidal ebb and flow of kernel fluid (Koch and Ma, 2017), all having relevance for assimilate supply and sink strength of the maize kernel. We propose that MRI, diffusivity modeling and other topological approaches can provide avenues for addressing long-standing questions in maize biology.

Materials and methods

Plant material and growth conditions

Plants were cultivated in a greenhouse under natural light supplemented with lamps to provide a 16/8 h photoperiod and an approximate light intensity of 800 µmol photons m⁻² second⁻¹. Temperature was controlled at 23°C (day) and 18°C (night). Plants were hand-pollinated for determination of developmental stages (days after pollination, DAP). Genotypes used in this study were the following: B73 (Zea mays), a teosinte morpho-type Tripsacum dactyloides (IPK-Genbank; accession number Zea 800), a perennial teosinte species Zea perennis (ZEA 832), popcorn type Zea mays subsp. everta var. purpuornis (ZEA 1166), mutant sweet4C (provided by Karen Koch, UF Gainesville), Waxy Maize A, a waxy-type corn Zea mays subsp. ceratina (ZEA 218), sweet corn (Zea mays subsp. saccharata var. dulcis, cv. Dippes Zuckermais and E-Mu-njan), and two glossy6 mutant lines (Maize genetics stock center #313A (line gl6) and #M841H (line gl6 wx1).

MRI experiments

MR imaging experiments were performed on the Avance III HD 400 MHz NMR spectrometer (Bruker Biospin, Germany). Three-dimensional (3D) water and lipid images were generated by using a chemical shift-selective spin-echo sequence as described in Munz et al. (2016). The water and lipid signals were acquired in an interleaved scheme. Chemical shift-selective calculated pulses were used for global excitation and refocusing of water or lipid protons. For generating the water images, the pulses were applied resonant on the water frequency, and with an offset of -1400 Hz for the lipid images. The field of views of $(13 \times 8 \times 8)$ mm, $(11 \times 7.5 \times 7.5)$ mm and $(11 \times 9 \times 9)$ mm were adjusted to the kernel size. The matrix sizes were correspondingly chosen as $(260 \times 160 \times 160)$, $(220 \times 150 \times 150)$ and $(220 \times 180 \times 160)$ 180), so that an isotropic resolution of 50 µm for every water and lipid image was achieved. The echo times (TE) were set as short as possible (7.5, 6.7 and 6.7 ms) to minimize signal reduction due to T2 relaxation. Repetition times of 850, 950 and 650 ms were used, so that the total measurement time for each of the three samples was around 24 h. The signal was averaged over four times to maximize signal-to-noise ratio. The processing of the NMR data was carried out using MatLab (MathWorks), the visualization of maize kernels was performed with AMIRA software (FEI Visualization Sciences Group). Three kernels per stage were analyzed.

Fourier transform infrared microspectroscopy

Kernel samples were frozen in liquid nitrogen and embedded in Tissue-Tek cryomolds and cryo-sectioned (3-12 µm) with a cryotome CryoStar NX7 (Thermo Fisher Scientific, Dreieich, Germany) according to Kawamoto et al. (2021) using adhesive foils. Tissue sections were lyophilized and stored in darkness at room temperature until analysis. Imaging was performed using a Hyperion 3,000 Fourier transform infrared (FTIR) microscope (Bruker Optics, Ettlingen, Germany) coupled to an Invenio S FTIR spectrometer (Bruker Optics) with an internal mid-infrared source. The focal plane array detector (64 × 64 pixel) was used in ATR mode. The imaging system was purged with dry air continuously. FTIR images were recorded in the spectral range of 3900 cm⁻¹ to 800 cm⁻¹ at a spatial resolution of 2-4 µm and a spectral resolution of 6 cm⁻¹ using a $20 \times (0.5 \,\mu\text{m} \text{ digital resolution})$ infrared magnification ATR objective (Bruker Optics). Each spectrum comprised 64 coadded scans. A reference of a single focal plane array window in the empty light path was acquired before image acquisition and automatically subtracted from the recorded image by the software OPUS (Bruker Optics). Atmospheric absorptions of water vapor and CO₂ were corrected by OPUS during image acquisition. Target regions were selected according to the visual image and spectra were exported into Matlab (2019b, The Mathworks Inc., USA). Exported spectra were vectornormalized in preparation for modeling. Representative spectra of waxes, cutin and polysaccharides (carbohydrates) were taken from Heredia-Guerrero et al. (2014). These were modeled into the exported tissue spectra using the spectral region of 3700–2600 cm⁻¹ to identify compositional representation of features by a constrained least squares fitting function. The predicted coefficients were used as an indicator for the dominance of associated features.

Short-term oxygen treatment in planta

At 18 DAP, kernels on an intact ear (enclosed within a transparent plastic chamber) were aerated with gas mixtures (combined by a multi gas controller, PCU10 MIX 2K, HTK Hamburg, Germany) containing either atmospheric oxygen levels (21 vol%), 30 vol% oxygen or 10 vol% oxygen. The same procedure was tested and applied earlier (Rolletschek et al. 2005). Oxygen concentration inside chambers was checked for accuracy using microsensors (NTH-PSt7-02 needle sensor connected to Microx-4, PreSens GmbH, Germany) placed inside the chamber. Regensburg, Time-course samples were harvested after 30 min, 2, 4, 8, 12 and 24 h of treatment. Each sample was frozen in liquid N₂ and stored at -80°C until analysis. For each time point, there were five biological replicates used for metabolite analysis and three to five used for RNA analysis. Each replicate sample consisted of at least three kernels. The experiment was started at 8 AM, and all sampling was done during the light phase of diurnal growth.

Long-term oxygen treatment in vitro

The High-O₂ treatment was applied to kernels grown in vitro during the developmental period of 10 to 27 DAP. For the culture, cobs were harvested at 5 DAP and up to 15 kernels were dissected under sterile conditions as in Gengenbach and Jones (1994). Individual kernels attached to cob segments were transferred to in vitro culture tubes (Duchefa Biochemie, Netherlands) each with a sterile 2 cm deep block of rock wool (Grodan Vital, Grodan, Canada). Two ml of culture medium was used in each tube and the explants were embedded into the rock wool. The medium was prepared following Glawischnig et al. (2000), and contained per liter 80 g of sucrose, 4.33 g of Murashige-Skoog salts, 2 g of Asn monohydrate, 400 µg of thiamine hydrochloride, and 10 mg streptomycin sulfate, or, for the labeling experiment, 2.5% of the sucrose as $^{13}C_2$ -sucrose and 2 mM $^{15}N_2$ -Gln. Medium was adjusted to pH 5.8 before sterile filtration. Explants were incubated at 23°C in the dark for five days using isotope-free media. After this period, the kernel segments were transferred to fresh trays and incubated for an additional 17 days at 23°C/18°C (day/night). Sample trays were kept inside chambers aerated with gas mixtures containing either atmospheric (21 vol%) or elevated oxygen levels (30 vol%). Oxygen concentration inside the chamber was continuously monitored using microsensors (NTH-PSt7-02 needle sensor, PreSens GmbH). After 17 days of treatment, kernels were removed, directly frozen in liquid N₂, and stored at -80°C until analysis. In the experiment with

labeled substrates, embryos and endosperms were separated and weighed before freezing in liquid N₂.

Microsensor experiments and histology

Oxygen profiling was done using oxygen-sensitive microsensors in a procedure described earlier (Rolletschek et al., 2005). After measurement, the kernel was dissected along the measured transect, and imaged photographically. Starch staining with lodine-potassium iodide solution was done as in Rolletschek et al. (2005). At least three individual kernels were measured per stage and genotype.

Respiratory assays

For analyzing embryo- and endosperm-specific respiration rates, we used a fluorescence ratiometric-based method (Tschiersch et al., 2012). Briefly, the kernel was cut in two halves and an oxygen-sensitive sensor foil was placed on the sample surface. Based on the localized change in fluorescence signal (= oxygen concentration) over time, the local oxygen consumption (characteristic of embryo and endosperm) was estimated for five individual kernels. Respiratory activity of intact kernels was measured as oxygen uptake rate of kernels placed in wetted, gas-tight vials (Munz et al., 2017). Rates of respiratory oxygen uptake were determined for five individual kernels from the change in sensor signal over time using linear regression models normalized to kernel fresh weight.

Biochemical analysis

Frozen kernels (five biological replicates each consisted of three kernels) were used for metabolite profiling, applying the procedure exactly as in Radchuk et al. (2021). In short, metabolic intermediates were extracted using methanol-chloroform-water mixtures. Soluble sugars were measured using ion chromatography coupled to amperometric detection (Guendel et al., 2018). All other intermediates were measured by ion chromatography (ICS-5000⁺) and UPLC (Vanquish Focused), both coupled to QExactivePlus hybrid quadrupole-orbitrap mass spectrometer (all instruments from Thermo Scientific, Dreieich, Germany). Chromatographic and detection schemes are given in Supplementary Method S1. Further details on batch processing and compound identification using the untargeted metabolomics workflow are given in Radchuk et al. (2021). Ethanol content in frozen, pulverized material was determined following extraction with tri-n-butyl phosphate using a photometric assay based on dichromate oxidation (Seo et al., 2008). The contents of starch, lipid, protein, and ash were measured in freeze-dried pulverized samples using a near-infrared spectroscope (MPA; Bruker), calibrated according to the supplier's protocol.

μ-CT and data analysis

Fresh kernels (B73) were scanned using a Phoenix Nanotom S μ -CT system (General Electric, Heidelberg, Germany) on a 12-bit 2304 \times 2304 detector with voxel resolutions of 5 μ m

at 55 kV and 229 kA. In total, 1,600 projection images were captured per sample (two kernel samples in total) with an average of two scans per projection and an exposure time of 500 ms, resulting in 27 min scanning time for each sample. The X-ray shadow projection images were reconstructed using a mathematical algorithm based on the filtered back-projection procedure implemented in the Phoenix CT Software (GE inspection Technology, Germany).

Oxygen diffusivity of porous pericarp

Three small regions $(200 \times 200 \times 200 \ \mu m^3)$ of the porous pericarp from each X-ray reconstructed image stack of maize kernels were cropped and segmented into cells and intercellular spaces using Otsu's thresholding to create a three-dimensional (3D) geometric model of the tissue and used to compute the effective oxygen diffusivity using a voxel-based numerical diffusion model (Ho et al., 2011). In the simulations, an oxygen concentration difference of 2 kPa was applied over the thickness of the 3D tissue geometry. Cells and air spaces were assigned oxygen diffusivity values of water and air, respectively. The diffusion flux through the tissue was computed, and the effective oxygen diffusivity was calculated using Fick's law of diffusion from the flux and the applied oxygen concentration gradient over the tissue sample.

Porosity estimation

The porosity of tissues was calculated from the original μ -CT images (at 5 μ m voxel resolution), where Porosity = volume of pore space/volume of whole tissue type. If no pores were evident at tissues at the given resolution, we indicated 0% porosity for them.

Reaction—diffusion modeling of oxygen transport in maize

To save computational memory and time, the voxel size of the reconstructed X-ray images was increased from 5 µm to 40 μm. The μ-CT scan of a maize kernel was segmented to obtain a volumetric geometrical model of the kernel distinguishing the different tissues including outer pericarp, porous pericarp, embryo, and endosperm. Resolution downsizing and segmentation of μ-CT images were conducted in Avizo 2020.1 (Thermo Fisher Scientific, Waltham, USA). A gradient image of the porous pericarp region and the remaining regions was created by a texture classification operation on one image slice, then the gradient image was used for watershed segmentation of the 3D stack to obtain the porous pericarp region. The embryo region was manually segmented using interpolation and warping operations. A reaction-diffusion model was applied to simulate the oxygen distribution in the intact maize kernel resulting from diffusion and respiration, subjected to atmospheric boundary conditions (21 kPa oxygen at 25°C) to the surface of the kernel. Effective diffusivity values were assigned to the different tissues. The anisotropy of the oxygen diffusivity with each region was neglected. The computed effective oxygen

diffusivity was applied to the porous pericarp region. Diffusivity of the embryo was computed assuming it a simple porous material, of which the effective diffusivity has a weighted value of diffusivity in gas and water balanced by porosity (Nugraha et al., 2021). The porosity of the embryo was computed from the segmented high-resolution μ -CT image and was found to be very low (0.026%). In the endosperm, the high local content of starch was accounted for (Zhang et al., 2016) by using an approximate oxygen diffusivity value $(1.0 \times 10^{-11} \text{ m}^2 \text{ s}^{-1})$ (Arvanitoyannis et al., 1994). Gradients in embryo diffusivity due to variations in starch and water content were explored, but these did not affect the overall oxygen gradients in the kernel. The diffusivity of the outer pericarp was difficult to obtain. Therefore, the sensitivity of the oxygen distribution to the value of the diffusivity of outer pericarp was evaluated using simulation with a range of values $(5.0 \times 10^{-9} \text{ to } 1.0 \times 10^{-11} \text{ m}^2 \text{ s}^{-1})$. Finally, the diffusion resistance of the lipidous layer around the endosperm was not taken into account because (1) it is very thin while the resistance of the starchy endosperm is already high due to its very low diffusivity and thickness, and (2) there is a lack of permeability data of the layer. Indicative values of oxygen diffusivity have been reported for pear fruit peel (containing a cutin layer on top of dense epidermis and hypodermis) as $1.9 \pm 0.7 \times 10^{-10}$ m² s⁻¹ (Ho et al., 2008). This value is higher than that of the endosperm and in the range of pericarp values. Still, the lipidous barrier that becomes established during development is likely enforcing the hypoxic state of endosperm as it is predicted by the model.

The respiratory oxygen consumption was modeled by means of a Michaelis-Menten model with consumption rates determined in the oxygen sensor experiment. The mitochondrial K_m value was assumed to be equal to $0.14 \,\mu\text{M} \, (1.02 \times 10^{-2} \, \text{kPa})$ (Verboven et al., 2013). The 3D model of the maize kernel was developed, and the reaction–diffusion model equations were solved using a finite volume method implementation in Matlab (Ho et al., 2011).

RNA extraction and Rt-qPCR

Total RNA was isolated from kernels (18 DAP) using Trizol/ chloroform, purified by RNeasy Plant Mini Kit (Qiagen) and treated with DNase I (New England Biolabs). RNA of 800 ng were used for cDNA synthesis. One µl of the cDNA was applied as a template for RT-qPCR with CYBR green (Invitrogen). Primers for six hypoxia-core genes (Gasch et al., 2016) were created using Primer3 (primer3.ut.ee) (Supplemental Table S1). Specificity and efficiency of primers were checked via melting curve analysis. The PCR reaction was performed after an initial denaturation at 95°C/120 s followed by 40 cycles of 95°C/15 s, 58°C/30 s, 72°C/60 s. Estimates of transcript abundances, based on four biological replicates, each represented by three technical repetitions, were derived by applying the $2^{-\Delta\Delta Ct}$ method (Livak and Schmittgen, 2001). The reference sequence was the housekeeping gene actin1 (gene ID GRMZM2G126010).

Library construction and RNA-seq

RNA was extracted from the maize kernels at 18 DAP (five biological replicates with three kernels each) as described above. The libraries were produced using the TruSeq RNA Kit (Illumina, San Diego, USA) following the manufacturer's instructions and sequenced using an Illumina HiSeq $^{\rm TM}$ 2,500 device.

Data from RNA-seq were analyzed using the Galaxy platform (Goecks et al., 2010) on the UF HiPerGator supercomputing system. For quality control, raw reads were trimmed and processed by Trimmomatic and checked with FastQC. Reads passing quality control were mapped and aligned to the B73 reference genome (version 4) with HISAT2. Alignments were assembled by StringTie with reference annotations from the B73 maize inbred. After initial assembly of these mRNAs, StringTie-merge was used to generate a transcriptome database representing all transcripts from the reference genome that were also present in any of the samples studied here. This database thus included the map location and origin of each transcript. Annotations were further checked using GFFcompare. To identify transcripts differentially expressed between the control and Low-O2 or High-O₂ treatments, FeatureCounts was used to quantify reads per transcript and DESeq2 to test differential expression. Default settings were used in all applications. Heat maps were constructed using Heatmap2. Kernel tissue expression data were from Doll et al. (2020). Pathway enrichment analysis and visualization were done as described by Reimand et al. (2019). The gene co-expression network was constructed as per Sanclemente et al. (2021).

Statistics

Mathematical calculations were performed using Excel 2019 (Microsoft Corp., Redmond WA, USA), and statistical analyses using either software MATLAB (version R2019b, http://www.mathworks.com) or RStudio (v. 1.2.5042). Statistical tests (P < 0.05) and replicate numbers are as shown in figure legends. For parametric tests, normal distribution was tested using Quantile-Quantile-plots (RStudio, package: ggpubr 0.3.0); variance homogeneity was tested using Levene's test (RStudio, package: car 3.0-7). Test results are given in Supplemental Data Set S5.

Accession numbers

The RNA-seq raw data sets have been registered in NCBI under the following accession numbers: PRJNA823922; Voltage-depend anion channel protein2 (Zm00001d038840); 23.6 kDa Heat-shock protein (Zm00001d044874).

Supplemental data

The following materials are available in the online version of this article.

Supplemental Figure S1. Starch accumulation and water content in developing maize kernels (Supports Figure 1).

Supplemental Figure S2. Additional oxygen concentration profiles determined in individual maize kernels (Supports Figure 2).

Supplemental Figure S3. Representative oxygen concentration profiles determined in developing kernels of B73 (Supports Figure 2).

Supplemental Figure S4. Skeletonization of pore structure (colored in red) in embryo based on μ -CT (Supports Figure 3).

Supplemental Figure S5. Example of quantitative respiration mapping of maize kernels (Supports Figure 3).

Supplemental Figure S6. Computation of oxygen distribution in a maize kernel (Supports Figure 3).

Supplemental Figure S7. Analysis of the infrared finger-print region (Supports Figure 4).

Supplemental Figure S8. Expression analysis of hypoxiacore genes in maize kernels (B73, 18 DAP) analyzed using RT-qPCR (Supports Figure 5).

Supplemental Figure S9. The strongest high-O₂ gene responses in maize kernels and their sites of expression under normal aerobic conditions (Supports Figure 5).

Supplemental Figure S10. The strongest low-O₂ gene responses in maize kernels and their sites of expression under normal aerobic conditions (Supports Figure 5).

Supplemental Figure S11. The oxidative stress genes downregulated by high- O_2 in maize kernels and their sites of expression under normal aerobic conditions (Supports Figure 5).

Supplemental Figure \$12. Gene Ontology (GO) enrichment maps of all DEGs in response to oxygen availability (Supports Figure 5).

Supplemental Figure S13. Photographic image of in vitrogrown maize kernels (Supports Figure 7).

Supplemental Figure S14. Hierarchical clustering and heatmap of log2-fold changes in metabolite abundance (Supports Figure 7).

Supplemental Table S1. Primers used for RT-qPCR.

Supplemental Methods S1. Chromatographic and mass spectrometry conditions for the analysis of maize kernels.

Supplemental Movie S1. 3D surface rendering of maize kernel, derived from X-ray μ-CT.

Supplemental Movie S2. Rotating, 3D model of void space of maize kernel, derived from X-ray μ -CT.

Supplemental Movie S3. MRI-based three-dimensional (3D) visualization of the maize kernel interior and localization of lipids in endosperm and embryo.

Supplemental Data Set S1. Differential gene expression analysis.

Supplemental Data Set S2. Gene expression network with color-coded Excel sheets for gene annotations and identifiers.

Supplemental Data Set S3. Untargeted metabolite analysis of maize kernels grown *in planta*.

Supplemental Data Set S4. Untargeted metabolite profiling analysis of in vitro-grown maize kernels.

Supplemental Data Set S5. Statistical test results.

Acknowledgments

Thanks to F. Bouquet for help in experiments, P. Keil for help in statistics, and M. Grau and Dr. A. Börner (IPK-Genbank) for providing plant material.

Funding

H.R. and L.B. acknowledge funding by the Deutsche Forschungsgemeinschaft (grant no. 411666988). H.X., P.V., and B.N. acknowledge funding by the Research Council of the KU Leuven (grant C16/16/002) and the Research Foundation Flanders (FWO project I013518N). J.G. and K.K. acknowledge funding by the National Science Foundation-IOS-PGRP-1748105. H.X. is a Ph.D. student funded by the China Scholarship Council (grant number 201806850087).

Conflict of interest statement. None declared.

References

Arvanitoyannis I, Kalichevsky M, Blanshard JMV, Psomiadou E (1994) Study of diffusion and permeation of gases in undrawn and uniaxially drawn films made from potato and rice starch conditioned at different relative humidities. Carbohydr Polym 24(1): 1–15

Bernardi J, Battaglia R, Bagnaresi P, Lucini L, Marocco A (2019) Transcriptomic and metabolomic analysis of ZmYUC1 mutant reveals the role of auxin during early endosperm formation in maize. Plant Sci 281: 133–145

Borisjuk L, Rolletschek H (2009) The oxygen status of the developing seed. New Phytologist 182(1): 17–30

Breitkreuz KE, Allan WL, Van Cauwenberghe OR, Jakobs C, Talibi D, André B, Shelp BJ (2003) A novel γ-hydroxybutyrate dehydrogenase. Identification and expression of an Arabidopsis cDNA and potential role under oxygen deficiency. J Biol Chem 278(42): 41552–41556

Cho Y-H, Yoo S-D (2011) Signaling role of fructose mediated by FIN1/FBP in *Arabidopsis thaliana*. PLoS Genet **7**(1): e1001263

Chourey PS, Hueros G (2017) The basal endosperm transfer layer (BETL): gateway to the maize kernel. In: Larkins BA, editor. Maize Kernel Development. Wallingford, Oxfordshire: CABI Publishing. p. 56–67

Doll NM, Just J, Brunaud V, Caius J, Grimault A, Depege-Fargeix N, Esteban E, Pasha A, Provart NJ, Ingram GC, et al. (2020) Transcriptomics at maize embryo/endosperm interfaces identifies a transcriptionally distinct endosperm subdomain adjacent to the embryo scutellum. Plant Cell 32(4): 833–852

Dumont S, Bykova NV, Khaou A, Besserour Y, Dorval M, Rivoal J (2018) Arabidopsis thaliana alcohol dehydrogenase is differently affected by several redox modifications. PLoS One 13(9): e0204530

Duszyn M, Świeżawska B, Szmidt-Jaworska A, Jaworski K (2019) Cyclic nucleotide gated channels (CNGCs) in plant signalling-Current knowledge and perspectives. J Plant Physiol **241**: 153035

Food and Agricultural Organization of the United Nations (FAO) (2015). The impact of disasters on agriculture and food security. (Food and Agricultural Organization of the United Nations, Rome) Report I5128E/1/11.15

Friedman H, Meir S, Philosoph-Hadas S, Halevy AH (2003) Effect of octanoic acid on ethylene-mediated processes in Arabidopsis. Plant Growth Regul 40(3): 239–247

- Fukui, K., Arai, K., Tanaka, Y., Aoi, Y., Kukshal, V., Jez, J.M., Kubes, M.F., Napier, R., Zhao, Y., Kasahara, H., et al. (2022). Chemical inhibition of the auxin inactivation pathway uncovers the roles of metabolic turnover in auxin homeostasis PNAS USA 119, 32
- Gasch P, Fundinger M, Müller JT, Lee T, Bailey-Serres J, Mustroph A (2016) Redundant ERF-VII transcription factors bind to an evolutionarily conserved cis-motif to regulate hypoxia-responsive gene expression in Arabidopsis. Plant Cell 28(1): 160–180
- Gayral M, Elmorjani K, Dalgalarrondo M, Balzergue SM, Pateyron S, Morel M-H, Brunet S, Linossier L, Delluc C, Bakan B, et al. (2017) Responses to hypoxia and endoplasmic reticulum stress discriminate the development of vitreous and floury endosperms of conventional maize (Zea mays) inbred lines. Front. Plant Sci 8: 557
- **Gengenbach, B.G., and Jones, R.J.** (1994). *In vitro* culture of Maize Kernels. In: Freeling M, Walbot V, editors. The Maize Handbook. Springer Lab Manuals. New York, NY: Springer New York. p. 705–708
- Gizak A, Duda P, Wisniewski J, Rakus D (2019) Fructose-1, 6-bisphosphatase: from a glucose metabolism enzyme to multifaceted regulator of a cell fate. Adv. Biol 72: 41–50
- Glawischnig E, Tomas A, Eisenreich W, Spiteller P, Bacher A, Gierl A (2000) Auxin biosynthesis in maize kernels. Plant Physiol **123**(3): 1109–1120
- Goecks J, Nekrutenko A, Taylor J, The Galaxy Team. (2010). Galaxy: a comprehensive approach for supporting accessible, reproducible, and transparent computational research in the life sciences. Genome Biol 11(8):R86
- Guendel A, Rolletschek H, Wagner S, Muszynska A, Borisjuk L (2018) Micro imaging displays the sucrose landscape within and along its allocation pathways. Plant Physiol 178(4): 1448–1460
- Hackett SR, Zanotelli VR, Xu W, Goya J, Park JO, Perlman DH, Gibney PA, Botstein D, Storey JD, Rabinowitz JD (2016) Systems-level analysis of mechanisms regulating yeast metabolic flux. Science 354(6311): aaf2786
- Hammarlund EU, Flashman E, Mohlin S, Licausi F (2020) Oxygen-sensing mechanisms across eukaryotic kingdoms and their roles in complex multicellularity. Science **370**(6515): eaba3512
- Hannah LC, Boehlein S (2017) Starch biosynthesis in maize endosperm.
 In: Larkins BA, editor. Maize Kernel Development.
 Wallingford, Oxfordshire: CABI Publishing. p. 149–159
- **Hartman S, Sasidharan R, Voesenek LACJ** (2021) The role of ethylene in metabolic acclimations to low oxygen. New Phytol **229**(1): 64–70
- Heredia-Guerrero JA, Benítez JJ, Domínguez E, Bayer IS, Cingolani R, Athanassiou A, Heredia A (2014) Infrared and Raman spectroscopic features of plant cuticles: a review. Front. Plant Sci 5: 305
- Ho Q, Verboven P, Verlinden B, Lammertyn J, Vandewalle S, Nicolaï B (2008) A continuum model for metabolic gas exchange in pear fruit. PLoS Comput Biol 4(3): e1000023
- Ho QT, Verboven P, Verlinden BE, Herremans E, Wevers M, Carmeliet J, Nicolaï BM (2011) A three-dimensional multiscale model for gas exchange in fruit. Plant Physiol 155(3): 1158–1168
- Johann H (1942) Origin of the suberized semipermeable membrane in the caryopsis of maize. J Agric Res **64**(5): 275–282
- Kanwar O, Samtani H, Sanyal SK, Srivastava AK, Suprasanna P, Pandey GK (2020) VDAC And its interacting partners in plant and animal systems: an overview. Crit Rev Biotechnol 40(5): 715-732
- Kawamoto T, Kawamoto K (2021) Preparation of thin frozen sections from nonfixed and undecalcified hard tissues using Kawamoto's Film Method (2020). Methods Mol Biol 2230: 259–281
- **Kelliher T, Walbot V** (2012) Hypoxia triggers meiotic fate acquisition in maize. Science **337**(6092): 345–348
- Koch KE, Ma F (2017) Determinants of kernel sink strength. In: Larkins BA, editor. Maize Kernel Development. Wallingford, Oxfordshire: CABI Publishing. p. 190–203
- Lee TA, Bailey-Serres J (2019) Integrative analysis from the epigenome to translatome uncovers patterns of dominant nuclear regulation during transient stress. Plant Cell 31: 2573–2595

- **Lendzian KJ** (1982) Gas permeability of plant cuticles. Planta **155**(4): 310–315
- Leroux BM, Goodyke AG, Schumacher KI, Abbott CP, Clore AM, Yadegari R, Larkins BA, Dannenhoffer JM (2014) Maize early endosperm growth and development: from fertilization through cell type differentiation. Am J Bot 101(8): 1259–1274
- Li L, Du Y, He C, Dietrich CR, Li J, Ma X, Wang R, Liu Q, Liu S, Wang G, et al. (2019) A novel maize gene, glossy6 involved in epicuticular wax deposition and drought tolerance. J Exp Bot 70(12): 3089-3099
- **Licek J, Baron M, Sochor J** (2020) Comparison of MCFA and other methods of terminating alcohol fermentation and their influence on the content of carbonyl compounds in wine. Molecules **25**(23): 5737
- **Livak KJ, Schmittgen TD** (2001) Analysis of relative gene expression data using real-time quantitative PCR and the 2(-Delta Delta C(T)) method. Methods **25**(4): 402–408
- Ma W, Guan X, Li J, Pan R, Wang L, Liu F, Ma H, Zhu S, Hu J, Ruan J-L, et al. (2019) Mitochondrial small heat shock protein mediates seed germination via thermal sensing. Proc Natl Acad Sci USA 116(10): 4716–4721
- Meng X, Li L, Narsai R, De Clercq I, Whelan J, Berkowitz O (2020) Mitochondrial signalling is critical for acclimation and adaptation to flooding in *Arabidopsis thaliana*. Plant Journal **103**(1): 227–247
- Munz E, Jakob PM, Borisjuk L (2016) The potential of nuclear magnetic resonance to track lipids in planta. Biochimie 130: 97–108
- Munz E, Rolletschek H, Oeltze-Jafra S, Fuchs J, Guendel A, Neuberger T, Ortleb S, Jakob PM, Borisjuk L (2017) A functional imaging study of germinating oilseed rapeseed. New Phytologist **216**(4): 1181–1190
- Nugraha B, Verboven P, Janssen S, Hertog M, Boone M, Josipovic I, Nicolai B (2021) Oxygen diffusivity mapping of fruit and vegetables based on X-ray CT. J Food Eng **306**: 110640
- Olsen O-A (2020) The modular control of cereal endosperm development. Trends Plant Sci 25(3): 279–290
- Park J-E, Park J-Y, Kim Y-S, Staswick PE, Jeon J, Yun J, Kim S-Y, Kim Y, Lee Y-H, Park C-M (2007) GH3-mediated Auxin homeostasis links growth regulation with stress adaptation response in *Arabidopsis*. J Biol Chem **282**(13): 10036–10046
- Plaxton WC, Podesta FE (2006) The functional organization and control of plant respiration. CRC Crit Rev Plant Sci 25(2): 159–198
- Radchuk V, Tran V, Hilo A, Muszynska A, Gündel A, Wagner S, Fuchs J, Hensel G, Ortleb S, Munz E, et al. (2021) Grain filling in cereals relies on developmentally controlled programmed cell death. Communications Biology 4(1): 428
- Reimand J, Isser R, Voisin V, Kucera M, Tannus-Lopes C, Rostamianfar A, Wadi L, Meyer M, Wong J, Xu C, et al. (2019) Pathway enrichment analysis and visualization of omics data using g:profiler, GSEA, cytoscape and EnrichmentMap. Nature Protocol 14(2): 482–517
- Rolletschek H, Koch K, Wobus U, Borisjuk L (2005) Positional cues for the starch/lipid balance in maize kernels and resource partitioning to the embryo. Plant Journal 42(1): 69–83
- Rolletschek H, Weschke W, Weber H, Wobus U, Borisjuk L (2004) Energy state and its control on seed development: starch accumulation is associated with high ATP and steep oxygen gradients within barley grains. J Exp Bot **55**(401): 1351–1359
- Sala RG, Andrade FH, Westgate ME (2007) Maize kernel moisture at physiological maturity as affected by the source-sink relationship during grain filling. Crop Sci 47(2): 711-716
- Sanclemente M-A, Ma F, Liu P, Porta AD, Singh J, Wu S, Colquhoun T, Johnson T, Guan J-C, Koch KE (2021) Sugar modulation of anaerobic-response networks in maize root tips. Plant Physiol 185(2): 295–317
- Sasidharan R, Schippers JHM, Schmidt RR (2021) Redox and lowoxygen stress: signal integration and interplay. Plant Physiol **186**(1): 66–78

- Schmidt RR, Weits DA, Feulner CFJ, van Dongen JT (2018) Oxygen sensing and integrative stress signaling in plants. Plant Physiol 176(2): 1131–1142
- Schwender J, König C, Klapperstück M, Heinzel N, Munz E, Hebbelmann I, Denolf P, De Bodt S, Redestig H, Caestecker E, et al. (2014) Transcript abundance on its own cannot be used to infer fluxes in central metabolism. Front Plant Sci 5: 668
- Seo HB, Kim HJ, Lee OK, Ha JH, Lee HY, Jung KH (2008) Measurement of ethanol concentration using solvent extraction and dichromate oxidation and its application to bioethanol production process. J Ind Microbiol Biotechnol 36(2): 285–292
- **Shelp BJ, Bown AW, Zarei A** (2017) 4-Aminobutyrate (GABA): a metabolite and signal with practical significance. Botany **95**(11): 1015–1032
- Shukla V, Lombardi L, Iacopino S, Pencik A, Novak O, Perata P, Giuntoli B, Licausi F (2019) Endogenous hypoxia in lateral root primordia controls root architecture by antagonizing auxin signaling in *Arabidopsis*. Mol Plant **12**(4): 538–551
- Sosso D, Luo D, Li QB, Sasse J, Yang J, Gendrot G, Suzuki M, Koch KE, McCarty DR, Chourey PS, et al. (2015) Seed filling in domesticated maize and rice depends on SWEET-mediated hexose transport. Nat Genet 47(12): 1489–1493
- Stelpflug S, Sekhon R, Vaillancourt B, Hirsch CH, Buell R, de Leon N, Kaeppler SM (2016) An expanded maize gene expression atlas based on RNA sequencing and its use to explore root development. Plant Genome 9(1). https://doi.org/10.3835/plantgenome2015.04.0025
- Sun Q, Li Y, Gong D, Hu A, Zhong W, Zhao H, Ning Q, Tan Z, Liang K, Mu L, et al. (2022) A NAC-EXPANSIN module enhances maize kernel size by controlling nucellus elimination. Nat Commun 13: 1–14
- Tsai CY, Salamini F, Nelson OE (1970) Enzymes of carbohydrate metabolism in the developing endosperm of maize. Plant Physiol **46**(2): 299–306
- Tschiersch H, Liebsch G, Borisjuk L, Stangelmayer A, Rolletschek H (2012) A visualization method for oxygen distribution, respiration and photosynthesis at a microscopic level of resolution. New Phytologist 196(3): 926–936
- Tzfadia O, Diels T, De Meyer S, Vandepoele K, Aharoni A, Van de Peer Y (2015) Coexpnetviz: comparative co-expression networks construction and visualization tool. Front. Plant Sci 6: 1194
- Van Dongen JT, Licausi F (2015) Oxygen sensing and signaling. Annu Rev Plant Biol 66(1): 345-367

- Van Dongen JT, Roeb GW, Dautzenberg M, Froehlich A, Vigeolas H, Minchin PEH, Geigenberger P (2004) Phloem import and storage metabolism are highly coordinated by the low oxygen concentrations within developing wheat seeds. Plant Physiol 135(3): 1809–1821
- Verboven P, Herremans E, Borisjuk L, Helfen L, Ho QT, Tschiersch H, Fuchs J, Nicolaï BM, Rolletschek H (2013) Void space inside the developing seed of Brassica napus and the modelling of its function. New Phytol 199(4): 936–947
- Wagner S, Steinbeck J, Fuchs P, Lichtenauer S, Elsässer M, Schippers JHM, Nietzel T, Ruberti C, Van Aken O, Meyer AJ, et al. (2019) Multiparametric real-time sensing of cytosolic physiology links hypoxia responses to mitochondrial electron transport. New Phytologist 224(4): 1668–1684
- Wang F, Chen Z-H, Shabala S (2017) Hypoxia sensing in plants: on a quest for ion channels as putative oxygen sensors. Plant and Cell Physiology 58(7): 1126–1142
- Watanabe N, Lam E (2008) BAX inhibitor-1 modulates endoplasmic reticulum stress-mediated programmed cell death in *Arabidopsis*. J Biol Chem **283**(6): 3200–3210
- Watanabe S, Matsumoto M, Hakomori Y, Takagi H, Shimada H, Sakamoto A (2014) The purine metabolite allantoin enhances abiotic stress tolerance through synergistic activation of abscisic acid metabolism. Plant Cell Environ 37(4): 1022–1036
- Weits DA, Giuntoli B, Kosmacz M, Parlanti S, Hubberten HM, Riegler H, Hoefgen R, Perata P, van Dongen JT, Licausi F (2014) Plant cysteine oxidases control the oxygen-dependent branch of the N-end-rule pathway. Nat Commun 5(1): 3425
- Weits DA, Kunkowska AB, Kamps NCW, Portz KMS, Packbier NK, NemecVenza Z, Gaillochet C, Lohmann JU, Pedersen O, van Dongen JT, et al. (2019) An apical hypoxic niche sets the pace of shoot meristem activity. Nature 569(7758): 714-717
- White MD, Kamps JJAG, East S, Kearney LJT, Flashman E (2018) The plant cysteine oxidases from *Arabidopsis thaliana* are kinetically tailored to act as oxygen sensors. Enzymology **293**(30): 11786–11795
- Young TE, Gallie DR, DeMason DA (1997) Ethylene mediated programmed cell death during maize endosperm development of wild-type and shrunken2 genotypes. Plant Physiol 115(2): 737–751
- Zhang Z, Zheng X, Yang J, Messing J, Wu Y (2016) Maize endospermspecific transcription factors O2 and PBF network the regulation of protein and starch synthesis. Proc Natl Acad Sci USA 113(39): 10842–10847